Use Authorization

In presenting this thesis in partial fulfillment of the requirements for an advanced degree at Idaho State University, I agree that the Library shall make it freely available for inspection. I further state that permission to download and/or print my thesis for scholarly purposes may be granted by the Dean of Graduate School, Dean of my academic division, or by the University Librarian. It is understood that any copying or publication of this thesis for financial gain shall not be allowed without my written permission.

Signature _____

Date _____

ATMOSPHERIC IMPACTS ON PLUME STABILITY

By

Bryan C. Nicholson

A thesis

submitted in partial fulfillment

of the requirements for the degree of

Master of Science in the Department of Geosciences

Idaho State University

Spring 2016

Committee Approval

To the Graduate Faculty:

The members of the committee appointed to examine the thesis of Bryan C. Nicholson find it satisfactory and recommend that it be accepted.

_____

Dr. Shannon Nawotniak,
Major Advisor

_____

Dr. Sarah E. Godsey,
Committee Member

_____

Dr. Alexander Urfer,
Graduate Faculty Representative

ACKNOWLEDGEMENTS

First, I extend the greatest thank you to my awesome advisor, Dr. Shannon Nawotniak, for taking me under her wing and shaping me into a proper volcanologist. Without her support, advice, and teachings, this thesis would not have been possible; I could not have asked for a better graduate advisor. I thank Dr. Sarah Godsey for the thesis support as well as my committee for the thesis review. I also want to thank my undergraduate advisor at California University of Pennsylvania, Dr. Kyle Fredrick, for providing both his guidance and a strong geologic background that would propel me into graduate school.

I also extend thanks to the ISU Geoscience administration, especially Kate Zajanc and Melissa Neiers for the travel and policies support; and Diana Boyack for the DML and printing support.

Thank you to Keith Weber for both connecting me with and providing job opportunities that supported me at ISU after my funding had dried up. I also thank Alexa Van Eaton for the correspondence that led me to improved ATHAM visualizations.

Lastly, but certainly not least, I thank my friends, family, and loved ones for the continued support that helped me get to this point and kept me sane throughout this journey.

Table of Contents

LIST OF FIGURES

LIST OF TABLES

ABSTRACT

Explosive volcanic eruptions almost always occur in an active wind field. This poses a challenge to hazard mitigation because wind has a complex influence on plume stability. Specifically, there is evidence that different ratios of mass eruption rate to ambient wind may cause the plume to become more or less stable, but the actual thresholds of these stability regimes are unknown. The transition between stable and unstable plumes depends on eruption column characteristics controlled by conditions at the volcanic vent and in the surrounding atmosphere. Since column stability determines the types of hazard associated with a volcanic eruption, there is a need to quantify the transition between stable and unstable eruptions. I investigate atmospheric impacts on plume stability thresholds using ATHAM (Active Tracer High-resolution Atmospheric Model) to simulate volcanic eruptions in 3-dimensions in no-wind and with-wind environments under different atmospheric profiles. The mass eruption rate (MER) is a key parameter for constraining plume stability as it is generally considered a first-order control on column height, and is controlled via ejection velocity and vent size. There are significant differences in plume rise heights between eruptions in high and low latitudes, with eruptions in tropical latitudes reaching plume heights 1.3-1.5x higher than their high-latitude counterparts due to the height of the tropopause. Wind can stabilize plumes that were unstable in the no-wind case by increasing the rate of ambient air entrainment and, therefore, increasing local buoyancy. Conversely, plumes may become unstable with too much wind; in that case, they are blown over to produce large pyroclastic

flows with low phoenix clouds. Wind-induced instability is a new concept in volcanic plume modeling and has significant implications for future hazard analyses.

Chapter 1: Introduction

1.1: Statement of Problem

Hundreds of millions of people throughout the world live on or in the vicinity of volcanoes (Tilling and Lipman, 1993), which poses a challenge for hazard mitigation. Ash column stability plays a significant role in the type of hazards presented by a given eruption. A stable, buoyant plume (Fig. 1) has successfully entrained and heated enough of the ambient air to rise buoyantly into the atmosphere (Kaminski and Jaupart, 2001). Hazards associated with stable volcanic eruptions include threats to aviation safety and infrastructure collapse from overloading of ash deposits.

For an unstable eruption (Fig. 2), where the erupting mixture cannot achieve positive buoyancy, the column will collapse to form a dangerously hot, fast, ground-hugging mixture of toxic gases and ash debris known as a pyroclastic density current (PDC). PDCs can flow down along the flanks of the volcano and spread out from its base, threatening nearby inhabitants. The most severe threats from a PDC include their density, velocity, and temperature. Autopsies performed on the bodies of victims from the Mount St. Helens eruption in 1980 indicated that death was caused instantly by high temperatures (400℃) and complete obstruction of the airways by ash (Eisele et al., 1981). Other victims suffered asphyxia, inhalation injuries and severe thermal injuries to skin (Spence et al., 2007). For inhabitants taking shelter in Herculaneum during the AD 79 eruption of Vesuvius, extreme heat was the leading cause of death (Mastrolorenzo et al., 2001).

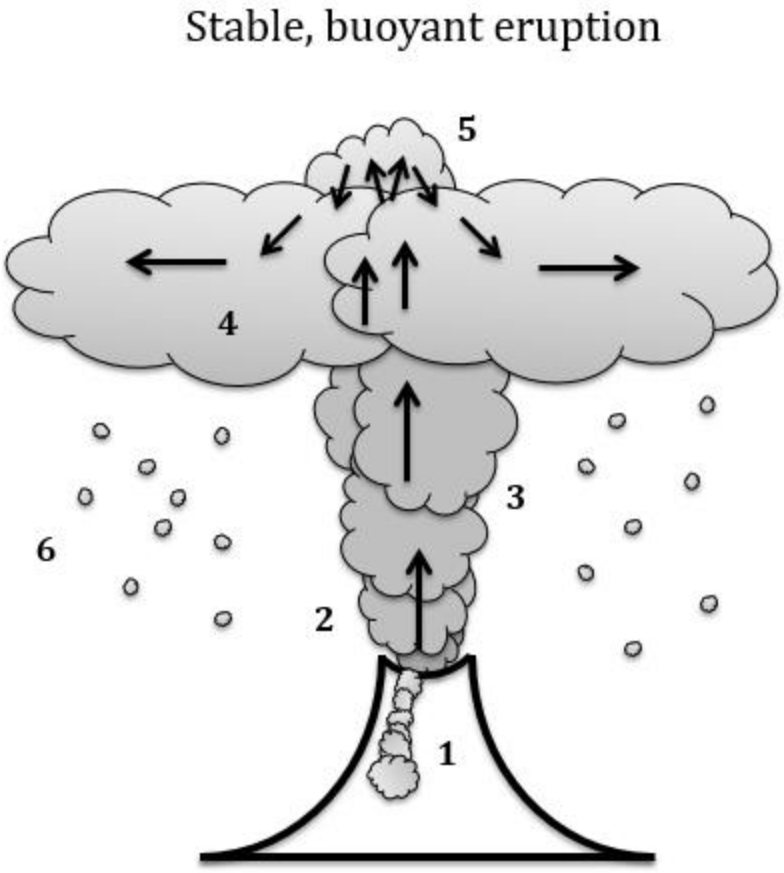

Figure 1: A cartoon example of a stable volcanic eruption. If the eruption column can achieve and hold positive buoyancy, then the column is considered stable. 1) Although it is considered a stable eruption, small ash flows can form out of the ash particles that failed to achieve positive buoyancy and tumble down along the flanks of the volcano. 2) The jet-thrust region is primarily driven by momentum and is where the ejecting material is normally denser than the surrounding atmosphere. 3) In the convective region, ambient air is drawn into the column and can further drive buoyant rise. 4) The umbrella region encompasses the laterally expanding phase of the plume where the rising ash particles meet a neutral buoyancy layer (NBL) in the atmosphere, often the tropopause or other thermal inversion. 5) The "overshoot" region is produced as rising ash particles exceed the NBL due to momentum, at which point the particles fall back down to the NBL. 6) Throughout the eruption ash particles are being sedimented from the plume and fall toward the surface. Sedimenting particles proximal to the rising column can become reentrained with the ambient air, effectively injecting cold, heavy material into the column and dampening buoyant rise.

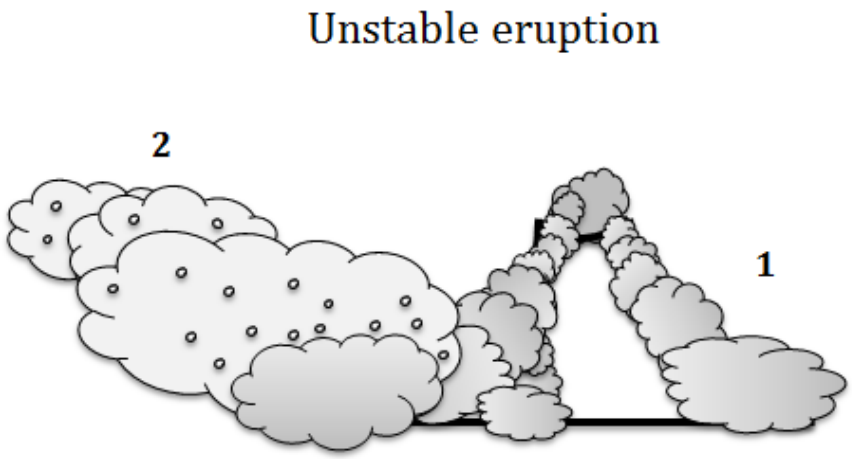

Figure 2: A cartoon example of an unstable volcanic eruption. 1) The erupting material fails to achieve positive buoyancy and collapses onto the surface as PDCs. 2) Along with PDC generation, some ash particles elutriate into the atmosphere to form a phoenix cloud, or coignimbrite.

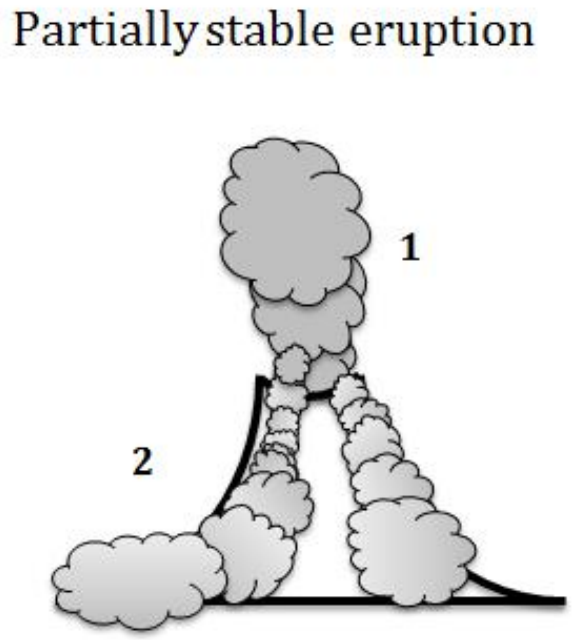

Figure 3: A cartoon example of a partially stable eruption. 1) A rising plume that cannot achieve and hold positive buoyancy for a significant time will at least partially collapse. Limited material in the rising plume will result in lower rise heights. 2) The material that could not achieve positive buoyancy will fall along the flanks of the volcano in flow currents or PDCs. PDCs are a considerable threat to any nearby inhabitants because the ash-debris mixture can have temperatures greater than 300 °C.

Between the stable and unstable end members are partially stable eruptions (Fig. 3), which encompass the transition between fully buoyant and fully collapsing ash clouds. In partially stable eruptions the column achieves some aspect of buoyant rise from mixing of ambient air, sometimes rising high into the atmosphere; however, there is insufficient mixing to support complete buoyancy, resulting in simultaneous PDC events (Kaminski and Jaupart, 2001). The transition between these stability behaviors and their hazards depend on the fluid dynamics of the eruption column, which is controlled by vent conditions (Woods, 1988; Cioni et al., 2003; Ogden et al., 2008) and ambient atmospheric conditions (Bursik, 2001; Van Eaton et al., 2012; Degruyter and Bonadonna, 2013).

The relationship between plume stability and hazards has driven significant research into the various parameters that affect plume stability. These parameters include upward vertical velocity (Woods, 1988), particle size (Bursik, 1989; Woods and Bursik, 1991), air and particle entrainment (Morton et al., 1956; Veitch and Woods, 2002; Suzuki and Koyaguchi, 2010), and the radius and density of the erupting plume (Woods, 1988). Additionally, wind is known to alter the plume trajectory, height, and stability in nearly all eruptions (Bursik, 2001; Koyaguchi et al., 2011); however, current literature has not reached a consensus on the exact controls or behavior regimes associated with plumes erupted into windy conditions. Other atmospheric characteristics can also impact the eruption column. For example, by comparing known eruptions and their respective atmospheres, Tupper at al. (2009) found significant differences in column heights (~9 km) between dry sub-polar and moist tropical atmospheres for similar weak volcanic eruptions.

Recent work in atmospheric influences on plume behavior involves computational modeling of volcanic eruptions in an effort to improve predictions of ash dispersal (e.g., Costa et al., 2006; Barsotti et al., 2008; Folch et al., 2009; Webster et al., 2010). Degruyter and Bonadonna (2013) used a 1-dimensional approach to model the impacts of some parameters on column stability, such as wind velocity, ejection velocity at the vent, and entrainment. Using a generalized regime diagram, their results show that wind can reduce maximum column height, prevent column collapse, and be the primary mechanism for entrainment, thus indicating that high winds are favorable from a hazards standpoint by reducing both PDC generation and maximum column heights. While the model gives a good first-order quantification of wind impacts on column stability, the simplified wind entrainment associated with limitations in 1-D prevents a more accurate representation of the underlying physics observed in nature (Degruyter and Bonadonna, 2013). Specifically, increased winds leading to a decreased column collapse rate may not hold true in all cases. For eruptions into high winds (> 15 m/s), column collapse may occur due to an overwhelming wind velocity (Kobs, 2009).

In this thesis, I investigate the impact of wind and the atmosphere on plume stability using a computational simulation of volcanic eruptions. I use ATHAM (Active Tracer High-resolution Atmospheric Model), a non-hydrostatic model that is formulated for use in a 2- or 3-dimensional grid-space (Herzog et al., 1998; Oberhuber et al., 1998). The model uses an implicit time stepping scheme and solves the full set of Navier-Stokes equations for momentum, mass and energy using a Large Eddy Simulation (LES) closure and explicitly solves for air entrainment

(Herzog et al., 1998). Additionally, ATHAM uses a microphysics module to describe condensation and formation of precipitation, which can affect plume dynamics (Herzog et al., 1998)

1.2: Objective and Hypothesis

I used ATHAM to systematically evaluate the effects of targeted parameters, such as mass eruption rate (MER), ambient wind speed, and atmospheric temperature, on plume stability. My objective was to use ATHAM to find stability thresholds resulting from the relative importance of MER and ambient wind speed under realistic atmospheric conditions.

Degruyter and Bondonna (2013) argue that increased ambient wind always increases plume stability. Conversely, Kobs (2009) (Fig. 4) proposed an approximate transition between wind-induced stability and wind-induced collapse. According to this hypothesis, for wind velocities sufficiently large relative to the MER a plume will lose stability and at least partially collapse because it is bent beyond its capacity for continued rise. In this thesis, I explore the idea of wind-induced collapse to identify the conditions under which it may occur. Wind-induced collapse may occur because heavier ash particles fall out and collectively produce a PDC from the deeply bent plume. This leads to the first hypothesis: *additional wind velocity on stable eruption columns can lead to column collapse.*

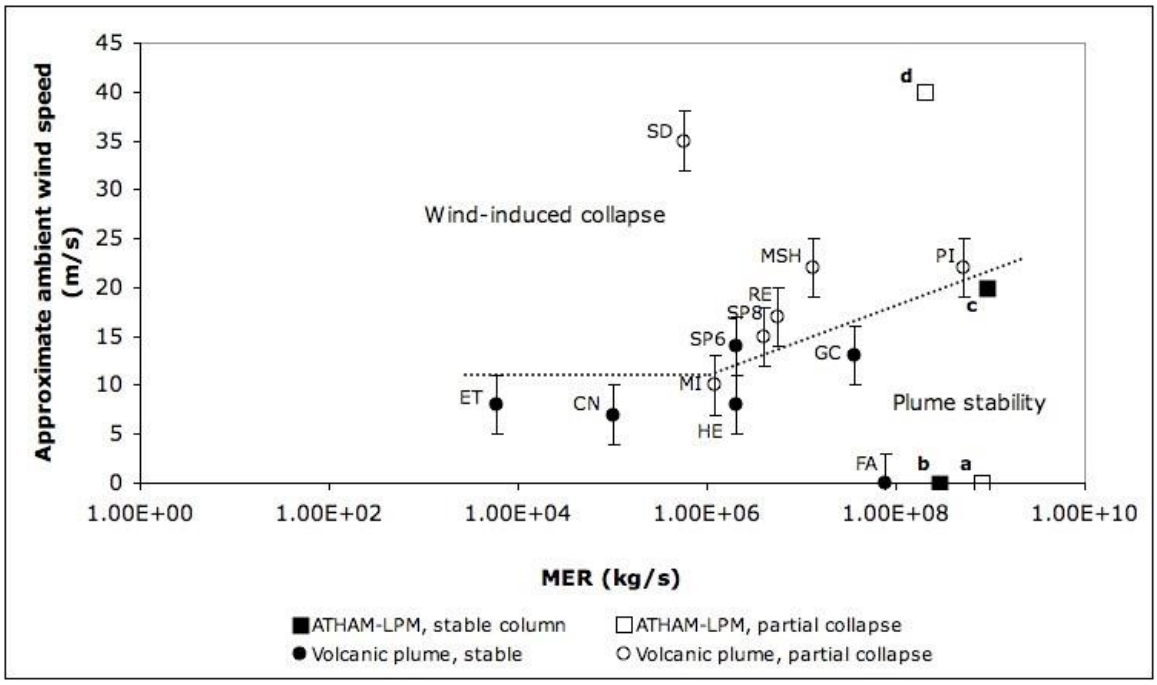

Figure 4: Partial column collapse as a function of MER and ambient wind velocity. This plot from Kobs (2009) shows a transition zone between stable and unstable (collapsing) volcanic eruptions as indicated by historical eruption events and ATHAM model runs. Additional model runs are completed in my study to further constrain this zone and to identify a secondary zone for "high" MERs, where high MER eruptions require additional wind velocities to remain stable.

I also examine the effects of other ambient atmospheric conditions, including temperature, tropopause height, and humidity, on column stability. Equatorial to low-latitude regions observe an average tropopause height of about 16 km, while the average height in polar regions is about 9 km (Hoinka, 1999). This range indicates that there is less potential air available for large-scale entrainment in high-latitudes, in addition to depressed convection, compared to low-latitude eruptions. This is important because there is little to no convection above the tropopause in the stratosphere. If the available air for entrainment is dampened in high-latitudes (>60°), then we should expect an impact on column stability. This leads to a second

hypothesis: *the tropopause height, which varies with latitude, has an impact on column stability because it limits the availability of space in the troposphere for large-scale air entrainment*. However, varying the tropopause with latitude inherently varies the atmospheric temperature and humidity. Therefore, I also test the impact of different atmospheric temperatures with a static tropopause height to determine whether the atmospheric temperature or tropopause height plays a more significant role in column stability.

If the first hypothesis is supported by this study, then it may be that high wind speeds during volcanic eruptions can stabilize some unstable eruptions and promote positive buoyancy as well as have the potential to destabilize eruption columns by knocking down the column, promoting PDC generation. Support for the second hypothesis presented in this study would indicate that an equivalent, stable eruption in low latitude regions may be unstable in polar regions due to the lack of available space in the troposphere for large-scale entrainment, reducing the ability of the plume to entrain ambient air for thermal expansion, a driver in maintaining buoyant rise. This has implications for generally broad-sweeping statements that link specific MERs to maximum column heights (e.g., Wilson et al., 1980; Wilson and Walker, 1987; Mastin et al., 2009; Degruyter and Bonadonna, 2012) indicating that atmospheric conditions and latitudinal locations of eruptions are critical when approximating the MER from maximum column height, and vice versa.

Chapter 2: Volcanic Ash Models, Hazards, and Column Stability

2.1: Volcanic Hazards

Tephra dispersed by explosive volcanic eruptions can travel over thousands of kilometers at velocities exceeding 100s of km/h (Carey and Sigurdsson, 1982). Significant hazards associated with volcanic eruptions include ash fall, lahars, pyroclastic density currents (PDCs), and lava flows. Ash from eruption columns and PDCs are often the most dangerous features associated with an explosive volcanic eruption with typical PDC travel velocities of 50 m/s (Ongaro et al., 2002). Issues related to ash fallout include: 1) causing or exacerbating respiratory problems to humans and animals, 2) damaging infrastructure, and 3) threatening aviation safety. PDCs can quickly devastate local areas by engulfing them in a hot pyroclast and gas mixture. These hazards can lead to death tolls in the thousands (El Chichón, Mexico 1982 – estimated 2,000 killed) to tens of thousands (Mt. Pelee, Martinique – estimated 29,000 killed) and can displace even greater numbers of people by destroying homes and other infrastructure (Witham, 2005). To reduce ash fallout threats, models are used to predict ash dispersal either in advance of or during an eruption, which can then be used to inform ground evacuations or air traffic reroutes.

2.2: Column Stability

For plinian volcanic eruptions, the dense initial mixture of gases and pyroclasts in the gas-thrust region is ejected from the vent at high velocities and

forms a turbulent jet (Fig. 5) where ambient air is rapidly entrained. The ambient air mixes with the plume material, is heated, and expands. As the column entrains cool ambient air, the hot pyroclasts warm the air and generate positive buoyancy, to create a convective, rising plume (Wilson, 1976; Wilson et al., 1978). The ash mixture at the vent can be multiple times denser than the surrounding atmosphere. However, the column density decreases with height as pyroclasts shed from the column and as air continues to become entrained and heated (Wilson and Walker, 1987). If the plume loses its upward momentum before sufficient entrainment occurs, such that the vertical velocity decreases to zero before positive buoyancy is reached, the mixture will form a collapsed fountain (Fig. 6) that feeds PDCs (Wilson and Walker, 1987).

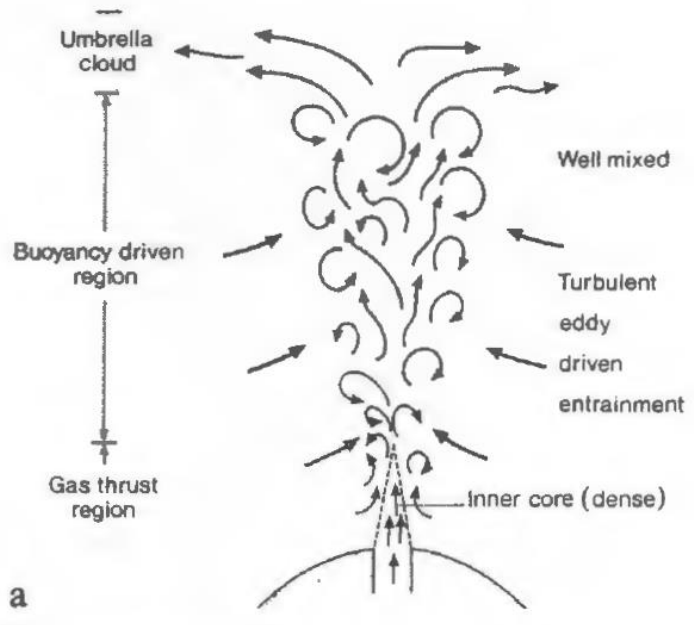

Figure 5: A drawing of the anatomy of an eruption column. The column can be broken down into three sections: the gas thrust, buoyancy driven, and umbrella cloud region. The initial gas thrust region is dominated by momentum force as it is ejected from the vent. The gas thrust region transitions into the buoyancy driven region upon achieving enough positive buoyancy to rise. Injection of the eruptive material into an atmosphere results in turbulent eddies that give rise to air entrainment into the column, which helps drive

buoyant rise through thermal rise and expansion. Generally, the plume expands radially as it continues to rise. With sufficient rise the plume may reach a point of neutral buoyancy with the atmosphere where the plume will spread laterally across this layer and form an umbrella region. This neutral buoyancy layer is often located along the tropopause, where the troposphere and stratosphere meet. Otherwise, the neutral buoyancy layer may be encountered below the tropopause. Note that the plume can encounter multiple neutral buoyancy layers as it rises, where ash particles can spread laterally at each layer. Figure 1 from Woods (1988).

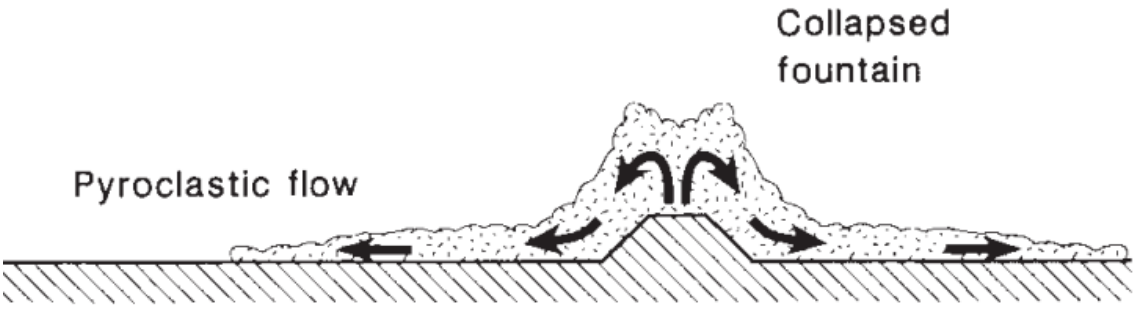

Figure 6: Drawing of a collapsed fountain eruption. The collapsed fountain is shedding pyroclastic flows laterally across the surface. Soon after such a scenario, a co-ignimbrite eruption cloud (not shown) may form from the pyroclastic flow as ash sheds off and rises buoyantly into the atmosphere. Figure 1 from Woods and Wohletz (1991).

Because stable and unstable eruptions present different challenges to hazard preparation and mitigation, quantifying the stability regimes and predicting the occurrence of PDCs versus stable, rising ash columns has been a significant area of study in physical volcanology (e.g., Sparks and Wilson, 1976; Wilson and Walker, 1987; Bursik and Woods, 1991; Kaminski and Jaupart, 2001; Ogden et al., 2008; Kobs, 2009; Degruyter and Bonadonna, 2013). Whether the eruption is buoyant and disperses ash primarily into the atmosphere, affecting aviation and distal (100+ km) populations, or is unstable and collapses into PDCs that strongly affect local inhabitants, plays a large role in determining the appropriate hazard response.

Several parameters are identified in literature as having an impact on column stability and are detailed in the following sections.

2.2.1: Entrainment

Entrainment occurs through turbulent mixing (Fig. 5) of the eruptive material, which brings in ambient air and decreases the bulk density of the plume. The transition between buoyant and collapse regimes is strongly affected by air entrainment (Woods, 1995; Kaminski & Jaupart, 2001). One of the first, large-scale quantification of entrainment is that of Morton et al. (1956). By assuming a top-hat velocity profile across the jet, they proposed that the entrainment rate at the edge of the jet was equal to the characteristic vertical velocity multiplied by an entrainment constant. In other literature (e.g. Ricou and Spalding 1961; Chen and Rodi 1980; Papanicolaou and List 1988; Suzuki and Koyaguchi 2010), this entrainment constant or coefficient was found to vary between plume regions, with lower entrainment coefficients near the vent and high coefficients with height.

2.2.2: Mass Eruption Rate (MER)

The mass eruption rate (MER) is a function of vent area, ejection velocity at the vent, and the bulk density of the erupting mixture. A higher MER for an explosive event indicates a more intense, high-energy eruption that ejects large volumes of material into the atmosphere. However, if the MER is too large, then the eruptive material may not be able to ingest sufficient ambient air to achieve bulk positive buoyancy, and a collapse event will occur (Wilson et al., 1980; Wilson and Walker, 1987; Kaminski and Jaupart, 2001). Wilson et al. (1980) state that the vent

radius and MER are approximately interchangeable because the vent radius strongly controls the MER. However, such a one-to-one relationship is an oversimplification (Degruyter and Bonadonna, 2013). Degruyter and Bonadonna (2013) used a 1-D plume model to quantify the key parameters that control the transition between buoyant and collapsing plumes. They presented a regime diagram for column stability that includes vent radius, ejection velocity, MER, entrainment, and wind velocity. They show that increased ejection velocity, wind velocity, and entrainment coefficients promote buoyant plumes, while increasing vent radius and the density difference between the ambient atmosphere and the eruptive material promotes plume collapse. For plume stability, they state that the most impactful parameter of the model is the ejection velocity while the parameter with the least impact is the density difference between ambient atmosphere and the jet. Perhaps the more important result presented by Degruyter and Bonadonna (2013) is that wind promotes buoyant rise and that MER does not always indicate the correct column stability because column collapse can occur whether MER is increased or decreased. This thesis builds upon this by using a 3-D numerical plume model, which explicitly solves for entrainment in both the vertical and horizontal directions (described further below) instead of using entrainment coefficients that parameterize sections of the plume to a single coefficient value, to further constrain the plume stability transition.

2.2.3: Wind

The influx of wind during an eruption can further impact plume stability. Real-world observations along with experimental quantifications show that wind can alter the plume shape and trajectory by deflecting, or bending, the plume (e.g. Bursik, 2001; Bonadonna et al., 2005) (Fig. 7). Wind effects include dampened maximum plume rise heights through dilution and lateral translation, and increased buoyancy of the plume due to increased air entrainment (Graf et al., 1999; Tupper et al., 2009; Degruyter and Bonadonna, 2012; Devenish, 2013).

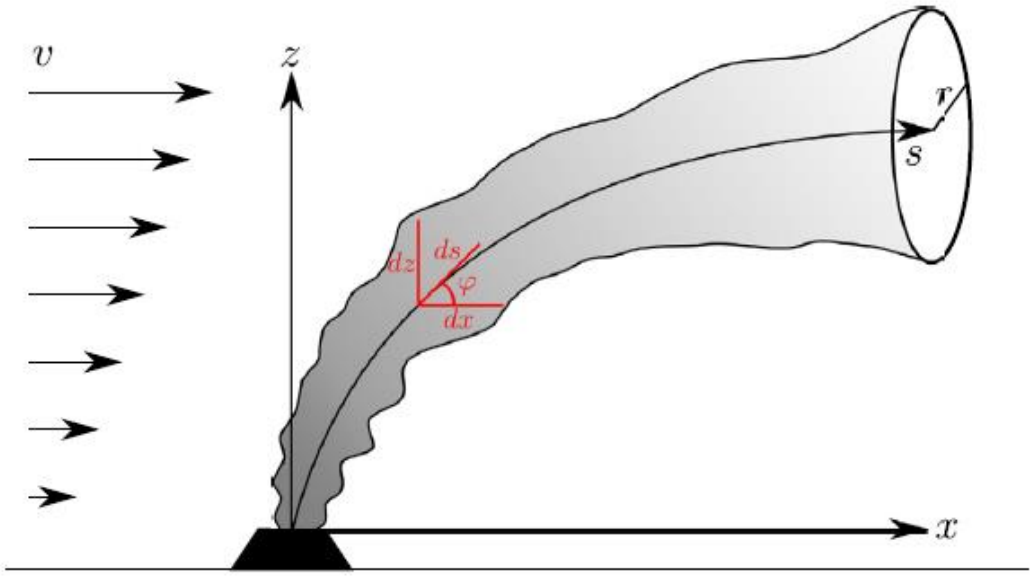

Figure 7: Drawing of a bent-plume with a plume-centered coordinate system. Figure 1 from Degruyter and Bonadonna (2013).

Because significant ambient wind is present in nearly all eruptions, it is important to quantify the effect of wind on plume behavior and stability. On small scales, wind can impact eddy structures while at large scale wind can alter plume

trajectory and morphology (Fig. 7) (Hewett et al., 1971; Wright, 1984; Bursik, 2001). Furthermore, high wind velocities may induce at least a partial plume collapse (Kobs, 2009). Models by Bursik (2001), Degruyter and Bonadonna (2013), and Kobs (2009) show that wind significantly improves air entrainment, can reduce the maximum height of the plume, and prevent plume collapse.

2.3: Tephra Transport and Deposition Models

Complex tephra models can more completely describe eruption column dynamics and tephra transport, but their sophisticated formulations increase model runtimes. On the other hand, simplistic models can quickly provide at least a first order understanding of tephra transport or column dynamics (e.g., Woods, 1988; Bursik, 2001) and are required for the fast solution times necessary for operational response models. Volcanic eruption models of the last few decades can be placed into one of three group types: integral, advection-diffusion-sedimentation (ADS), or simulation. Each model category has its own preferred application as well as model simplifications or assumptions.

2.6.1: Integral models

Early models dealing with the eruption column used a pseudo-fluid approximation in which solid ash particles and gases were assumed to be in thermal and mechanical equilibrium, allowing the whole mixture to be described as a bulk fluid (Wilson, 1976; Wilson and Walker, 1987; Sparks et al., 1997). Integral models use spatially integrated equations of motion to model tephra transport or deposition under steady state flow, describing the plume with equations of

conservation for mass, momentum and energy (Woods, 1988; Glaze and Baloga, 1996). Some of the earliest work with integral models is that of Morton et al. (1956) with buoyant plumes from smoke stacks, where they quantified the description of entrainment using a top-hat velocity profile and related entrainment rate at the plume edge to the vertical velocity. Some integral models, such as Carey and Sparks (1986) and Wilson and Walker (1987), use the wind to stretch and horizontally translate the neutral buoyancy region of the plume. Suzuki (1983) improved the description of near-vent deposition with a radially expanding column and a decreasing vertical velocity. Woods (1988) extended the work of Morton et al. (1956) to include a mix of pyroclasts and gases, thermodynamics between phases, and atmospheric stratification.

Integral models tend to show good first-order agreement with field deposits and plume shape under no-wind conditions. However, they are not robust enough to fully describe ash transport or full column dynamics within a wind field (Bonadonna et al., 2005). Integral models must often make simplifying assumptions about the eruption, such as steady state vertical flow. Instead of applying the full set of Navier-Stokes equations like in more complex simulations, integral models empirically derive an entrainment factor to address turbulence along the plume edge (Van Eaton, 2012). Thus, integral models generally limit the interactions between eruption columns and ambient wind through plume bending approximations (e.g. Bursik, 2001). In response to the importance of plume geometry relative to ambient wind, Bursik (2001) introduced a plume-centered coordinate system instead of the traditional Cartesian approach to model entrainment in a bent plume. This

approach, known as the BENT model, has since been adopted by a variety of integral and ADS models in order to improve their characterization of the plume shape in wind (e.g., Macedonio et al., 2008; Bursik et al., 2009; Degruyter and Bonadonna, 2013; Woodhouse et al., 2013).

2.6.2: Advection-Diffusion-Sedimentation models

Advection-Diffusion-Sedimentation (ADS) models focus on the transport and deposition of ash from an already in-air volcanic cloud (Suzuki, 1983). With such an initialization, the column dynamics are left unresolved (Van Eaton, 2012). The ADS equations are solved for ash transport and fallout using either a Lagrangian (for particle-tracking, e.g. Tanaka, 1994) or Eulerian (for tephra fallout, e.g. Costa et al., 2006) approach to model ash dispersion from an eruptive column. The Lagrangian formulation tracks the path of individual particles, while the Eulerian approach describes changes in concentration at fixed points in a grid (Fig. 8). However, recent computational advances allow for the treatment of ash dispersion and fallout using both approaches. ADS models (e.g., Hurst, 1994 [ASHFALL]; Searcy et al., 1998 [PUFF]; Bonadonna, 2005 [TEPHRA2]) typically initialize the eruption column as a vertical line source or borrow a curved approximation from BENT (Bursik, 2001) (Fig. 9) with variable mass distribution along the line (Bonadonna and Costa 2010).

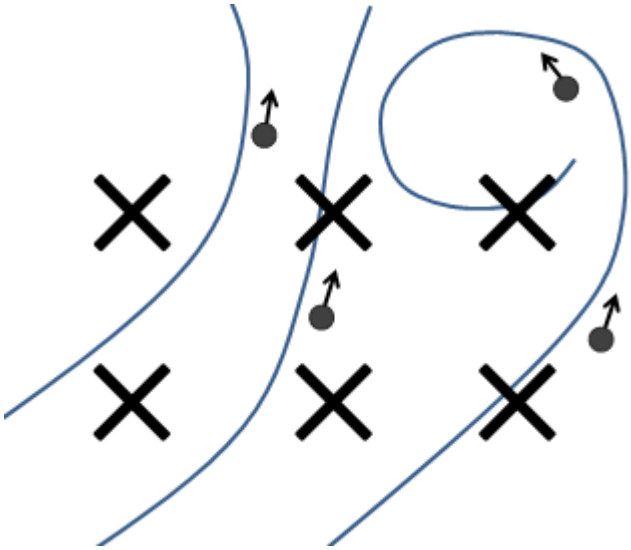

Figure 8: A 2D cartoon illustration of Eulerian and Lagrangian approaches. The X's represent grid points and the dots represent particles with travel direction. The lines show flow direction and eddy features. A pure Lagrangian approach focuses on individual particles and tracks their path through space whereas an Eulerian approach focuses on values of a fluid at each grid point (for example, ash concentration). These approaches can be combined to describe both a bulk fluid and individual particles within the fluid. To note, eddies are not resolvable at scales finer than the grid, what is shown is a simplification.

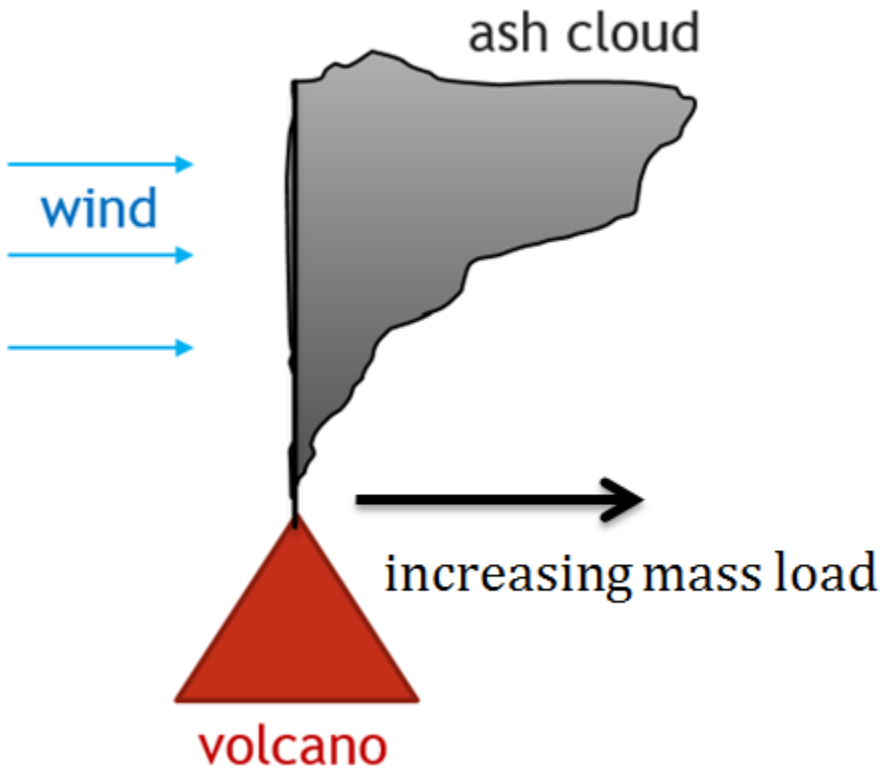

Figure 9: An illustration of ash dispersion under an ADS model given a vertical line source. The vertical line source, located directly above the volcano, represents the point from which ash originates in such ADS models. Generally, the ADS model assigns certain ash concentrations along the length of the line to approximate a lateral dispersion of the ash cloud downwind. Other models may use a bent-over plume approach (e.g. Bursik, 2001) to describe plume growth.

Given sufficiently detailed ambient wind fields, ADS models tend to excel when predicting in-air tephra dispersal at medial (~50 km) to distal (>100 km) ranges (e.g., Hurst and Turner, 1999; Connor et al., 2001; Costa et al., 2006). However, unresolved column dynamics in ADS models prevent any application to column stability. Due to their simplification of the eruption column above the vent, ADS models tend to break down when describing proximal deposits (Kobs, 2009). Specifically, because there is often no treatment of the eruptive column, there is

little to no description for entrainment of ambient wind, complex air flow in the near-vent area, or ash reentrainment into the plume (though this last is approximated by Ernst et al., 1996 and Sparks et al., 1997).

The quality of ADS model outputs is dependent on the accuracy of the ambient wind field used. FALL3D, an Eulerian model, uses a wind field from a meteorological limited area model (LAM) to forecast in-air atmospheric ash concentrations or ash loading at the ground during eruptions (Costa et al., 2006). ASHFALL, a 3D turbulent diffusion model, uses the most recent wind forecasts available to predict ashfall (Hurst and Turner, 1999). TEPHRA2 uses an altitude varying wind profile as user-input to calculate tephra transport and deposition (Bonadonna et al., 2005). The Lagrangian model PUFF, developed as a real-time ash plume tracking model for use in aviation safety, uses wind data from UNIDATA (Tanaka, 1994; Searcy et al., 1998; Yamamoto, 2002). One of the advantages of ADS models is that their runtimes are on the order of 1-10s of minutes, allowing for relatively quick forecasts of ash transport to inform emergency procedures, specifically air traffic hazard mitigation.

2.6.3: Simulations

Over the past 15-20 years, numerical simulations of volcanic eruption columns have been developed to characterize increasingly complex column dynamics via computational fluid dynamics (e.g., [ATHAM] Oberhuber et al., 1998; [PDAC] Ongaro et al., 2007). Simulations of volcanic eruptions solve the Navier-Stokes equations and focus on localized, microphysical dynamics of the eruption

column as opposed to the more distal predictions of ash transport and deposition often seen with ADS models. The plume is treated as a compressible multiphase flow in either 2- or 3D. While integral or ADS models have low computational cost, simulations often require many days of runtime, even on a distributed memory cluster. Recent work in volcanic eruption simulations include that of a) Suzuki et al. (2005), a 3-D model developed to investigate the impact of turbulent mixing on entrainment, b) the Pyroclastic Dispersal Analysis Code (PDAC) (Neri et al., 2003; Esposti Ongaro et al., 2007), which can simulate pyroclastic flows over realistic topography, and c) the Active Tracer High-resolution Atmospheric Model (ATHAM) (Oberhuber et al., 1998), which describes microphysical dynamics under realistic atmospheric conditions. The atmospheric emphasis in ATHAM, further described below, makes it ideal for investigating the impacts of various atmospheric effects on plume stability.

ATHAM is a non-hydrostatic model that uses an implicit time stepping scheme and solves the full set of Navier-Stokes equations for momentum, mass and energy using a Large Eddy Simulation (LES) closure (Herzog et al., 1998; Oberhuber et al., 1998; Herzog et al., 2003). This LES closure computes entrainment using turbulent exchange coefficients in both the vertical and horizontal directions, accounting separately for the vertical stratification of the atmosphere (Oberhuber et al., 1998; Herzog et al., 2003). For comparison, the work of Morton et al. (1956) assumes the entrainment coefficient to be constant for jets and plumes. However, this was later found to be inadequate since the radial expansion of a plume is greater than that of a jet, leading to different entrainment coefficients between

plume regions and with height (Wilson, 1976; Kotsovinos and List, 1977; Sparks, 1986; Woods, 1988; Suzuki and Koyaguchi, 2010, 2012). A primary strength of ATHAM is that it treats eruptive particles, such as fine ash and water vapor, as active tracers. This means that particles directly influence plume behavior, instead of simply being passively carried by the surrounding gas or being reduced to a simple pseudofluid. The active tracers strongly affect the dynamics of the column and are capable of undergoing phase changes throughout transport, such as condensation and freezing, which release latent heat into the plume. ATHAM assumes all of the tracers are in dynamic and thermal equilibrium with the bulk fluid such that any change in velocity or temperature is instantaneously exchanged between gas and solids; this assumption requires all particles to be sufficiently small so that any exchange in temperature or momentum between gas and particles is approximately instantaneous (Herzog et al., 1998). The largest clast size that can be included with this assumption is 1 mm diameter sized clasts for a Plinian type eruption (Bursik, 1989). However, work from Kobs (2009) provided ATHAM with a module that allows for inclusion of clasts >1 cm using the ballistic equations of motion. Previous work with ATHAM (e.g. Graf et al, 1999; Textor et al., 2004; Van Eaton 2012) gives output that demonstrates observable, intermittent fall and flow deposits that produce PDCs as well as a buoyant plume during the same eruption. ATHAM can also simulate fully collapsing eruptions in both 2- and 3D.

Simulations are computationally expensive, often requiring parallel processing for adequate runtimes. ATHAM, in particular, has runtimes on the order of hours to days, depending on the specified spatial resolution and length of the eruption. These

lengthy runtimes prevent such simulations from actively informing emergency operations in the case of a real-time volcanic eruption, which warrants response times on the order of 10s of minutes (Casadevall et al., 1996). Their usefulness lies in the research environment to analyze historic eruptions and to inform *a priori* inputs of source conditions for use in simplified ADS models.

Chapter 3: Atmospheric impacts on plume stability

3.1: Introduction

Ash column stability plays a significant role in the hazards associated with a volcanic eruption. A stable, buoyant ash plume that rises high into the atmosphere can threaten aviation safety and ground-based infrastructure, while an unstable, collapsing plume produces pyroclastic density currents (PDCs) potential of causing complete devastation. A partially stable plume, which represents a transition type between the two stability end members, can exhibit hazards of both. This stability transition and the accompanying hazards depend on the fluid dynamics of the eruption column, which is a function of vent conditions and ambient atmospheric conditions. Many factors have an impact on column stability, including vertical velocity (Woods, 1988), particle size distribution (Bursik, 1989; Woods and Bursik, 1991), air and particle entrainment (Morton et al., 1956; Veitch and Woods, 2002; Suzuki and Koyaguchi, 2010), vent overpressure (Ogden et al., 2008); wind velocity (Degruyter and Bonadonna, 2013), and the radius and density of the erupting plume (Woods, 1988).

The atmospheric profile, including ambient temperature and humidity, can also impact the plume; for example, Tupper at al. (2009) found an approximately 9 km difference in column heights between dry sub-polar and moist tropical atmospheres for otherwise identical volcanic eruptions. Additionally, wind alters the plume trajectory, height, and stability in nearly all eruptions (Bursik, 2001; Koyaguchi et al., 2011; Degruyter and Bonadonna, 2013). Recent 1D models suggest

that wind-enhanced entrainment is capable of stabilizing otherwise unstable plumes (Degruyter and Bonadonna, 2013), while preliminary 3D model outputs indicate that continuing to increase ambient wind speeds can cause a transition from stability-enhancing to destabilizing (Kobs, 2009).

3.2: Column Stability

For plinian volcanic eruptions, the dense initial mixture of gases and pyroclasts in the gas-thrust region erupts at high velocities as a turbulent jet. Whether the ash plume will rise buoyantly or collapse to form PDCs depends on the rate at which atmospheric air is entrained into the column to decrease the bulk density; this is a function of initial conditions of the eruption, such as mass eruption rate (MER), and atmospheric conditions. Degruyter and Bonadonna (2013) used a 1-D plume model to evaluate the sensitivity of key parameters that control the transition between buoyant and collapsing plumes. They presented a regime diagram for column stability that includes vent radius, ejection velocity, MER, entrainment, and wind velocity. According to the plume-centric 1D stability model, increased ejection velocity, wind velocity, and entrainment coefficients promote buoyant plumes, while increased vent radius and the density difference between the ambient atmosphere and the eruptive material promotes plume collapse, with ejection velocity as the most sensitive variable (Degruyter and Bonadonna, 2013). This is consistent with previous results indicating that small vent velocities (~100 m/s) tend toward column collapse (e.g. Wilson, 1976; Woods, 1988). The impacts of these parameters are further discussed in the following sections.

3.2.1: Entrainment

Entrainment efficiency determines the maximum height and dynamics of ash clouds (Morton et al., 1956; Woods, 1988; Kaminski et al., 2005; Suzuki and Koyaguchi, 2009). The first quantification of entrainment is that of Morton et al. (1956), who proposed that the entrainment rate at the edge of the jet was proportional to the average vertical velocity multiplied by an entrainment coefficient. Subsequent literature found that the entrainment coefficient varied between plume regions, with lower entrainment coefficients near the vent and higher coefficients with height (e.g., Ricou and Spalding, 1961; Chen and Rodi, 1980; Papanicolaou and List, 1988; Kaminski et al., 2005; Suzuki and Koyaguchi, 2010). Despite some variability in literature, the overall trend is that entrainment is more pronounced in buoyant plumes than in non-buoyant jets (Kaminski et al., 2005). Entrainment can be enhanced by wind since the plume will ingest some of the crossflow from an ambient wind field, leading to increased dilution, decreased column height, and bending (Hewett et al., 1971; Wright, 1984; Sparks et al., 1997; Bursik, 2001); this is incorporated into simple plume models by using a plume-centric coordinate system to reproject the Morton et al. (1956) entrainment model (Bursik, 2001). In contrast, the model used in this study explicitly solves for entrainment using computational fluid dynamics (Herzog et al., 1998).

3.2.2: Mass Eruption Rate (MER)

The mass eruption rate (MER) (Eq. 1) is calculated as the vent area (A) multiplied by the ejection velocity (v) and the bulk density of the erupting mixture (ρ).

$$\text{MER} = A\rho v \qquad (1)$$

A higher MER indicates a more intense, high-energy eruption that ejects larger volumes of material into the atmosphere. However, if the MER is too large, then the eruptive material may not achieve buoyant rise, and a collapse event will occur (Wilson et al., 1980; Wilson and Walker, 1987; Kaminski and Jaupart, 2001). Wilson et al. (1980) state that the vent radius and MER are approximately interchangeable because the vent radius strongly controls the MER. However, such a one-to-one relationship is an oversimplification (Degruyter and Bonadonna, 2013). While MER is a significant factor in column stability, it is expressed via a complex relationship; column collapse can occur with both high and low MERs (Degruyter and Bonadonna, 2013).

3.2.3: Wind Effects

Wind can alter the shape and trajectory of the plume, bending it in the downwind direction (e.g., Hewett et al., 1971; Wright, 1984; Sparks et al., 1997; Bursik, 2001; Bonadonna et al., 2005). Wind effects include dampened maximum rise heights through dilution and lateral translation of the plume, and increased buoyancy of the plume due to increased air entrainment (Graf et al., 1999; Tupper et al., 2009; Degruyter and Bonadonna, 2012; Devenish, 2013). On small scales, wind

can impact eddy structures, while at large scales wind can alter the entire plume trajectory (Hewett et al., 1971; Wright, 1984; Bursik, 2001). Wind significantly improves air entrainment via increased ambient air ingestion into the plume and can reduce the maximum height of the plume through dilution and cloud translation (Kobs, 2009; Degruyter and Bonadonna, 2013). This is significant because, while improved entrainment in a wind field may lead to a more buoyant plume, that same wind can bend the plume and reduce its maximum achieved height, decreasing bulk buoyancy through over-dilution. Taken to the extreme, preliminary model results suggest that very high wind velocities relative to MER may induce at least partial plume collapse by knocking over the plume (Kobs, 2009).

3.3: ATHAM Modeling

We use the Active Tracer High-resolution Atmospheric Model (ATHAM) to investigate wind-related plume stability in 3D. ATHAM is a non-hydrostatic model formulated for use in 2- or 3-dimensional grid-space that describes microphysical dynamics under realistic atmospheric conditions (Herzog et al., 1998; Oberhuber et al., 1998). The model uses an implicit time stepping scheme and solves the full set of Navier-Stokes equations for momentum, mass and energy using a Large Eddy Simulation (LES) closure, explicitly solving for air entrainment (Herzog et al., 1998). ATHAM can treat erupted particles as active tracers, where the particles are allowed to interact with the volcanic plume instead of being passively transported by the plume. ATHAM can be set to a few different modes: 2D cylindrical, 2D Cartesian, and full 3D Cartesian. While the 2D Cartesian mode in ATHAM can be used with wind,

we initialize ATHAM for 3D to study more robust wind effects at the expense of computational runtime (Herzog et al., 2003; Van Eaton, 2012). Previous work with ATHAM (e.g., Graf et al, 1999; Textor et al., 2004; Van Eaton, 2012) demonstrates its potential to model co-occurring PDCs and buoyant plumes. The primary goal of this work is to constrain the column collapse transition through a large suite of ATHAM simulations targeting specific parameters that impact plume stability, including vent size, vent velocity, and ambient atmospheric conditions, thus providing insight to the conditions that give rise to buoyant or collapsing volcanic plumes.

3.4: Methods

The primary ATHAM parameters included here for testing impact on plume stability are the mass eruption rate (MER), ambient wind, and atmospheric conditions such as tropopause height, temperature, and relative humidity. Atmospheric data was acquired from radiosonde data from the University of Wyoming online database collection (Atmospheric Soundings, 2015). We selected two weather stations, one from Trinidad and Tobago and the other from Inuvuk, Alaska, for examples of low and high latitude atmospheric conditions. For each, we averaged the temperature and humidity profiles for a month at each station to obtain characteristic curves (Figs. 10 and 11); Trinidad and Tobago was averaged over a wet month (January, 2015), while Inuvuk was averaged over a dry one (June, 2015). The wind velocity information from these stations was compiled in the same manner and one wind profile was produced that was used for each atmosphere, with slight adjustments to ensure that the maximum wind velocities were at or

around tropopause height (~10 km for the cold-dry profile and ~16 km for the warm-wet profile). This wind profile, which initially had a 10 m/s speed at the tropopause, was re-scaled for peak tropopause speeds of 20, 30, and 40 m/s (Fig. 12). This single set of wind profiles was used in both temperature/humidity profiles. Atmospheric profiles from different latitudes may demonstrate variable tropospheric impacts on column stability. Specifically, column stability may be affected by depressed tropopause in high latitudes, atmospheric water vapor, or difference in ambient temperature. A low altitude tropopause reduces maximum column height (Tupper et al., 2009), which may dampen entrainment in the troposphere, leading to decreased plume stability; conversely, air associated with low tropopause areas is relatively cold and dense, which may enhance relative buoyancy. In addition to our suite of 3D simulations, a small set of 2D runs were also completed. The 2D eruptions were compared with the same 3D eruptions to investigate any significant differences in plume stability and maximum height to test the effectiveness of ATHAM-2D to predict the stability and height of ATHAM-3D eruptions.

Each atmospheric profile was applied to eruptions with vent velocities of 100, 200, 300, and 400 m/s. This velocity range is consistent with exit velocities from previous work (e.g., Wilson et al., 1980; Woods, 1988; Carazzo et al., 2008). The diameter of the vent is varied between 100, 250, 1000, and 3000 meters for each vent velocity in order to calculate a range of MERs. Since the bulk density of the eruptive material has a comparatively low impact on the MER (Degruyter and Bonadonna 2013), it is kept the same (3 kg/m^3) between each simulation, which is

consistent with bulk densities used in similar ATHAM simulations (2-4 kg/m^3) by Van Eaton et al. (2012). The following input values were kept as an arbitrary default, remaining the same between each run: the specific gas concentration at the vent is 6 wt%, leaving 94 wt% as the specific particle concentration at the vent, which is an acceptable value (Carazzo et al., 2008); two particle tracers for ash are used, each with densities of 2500 kg/m^3, occupying 47 wt% at the vent, and diameters of 3.15 μm and 12.5 μm. A list of all simulations completed in 2- and 3D is given in Tables 1-4.

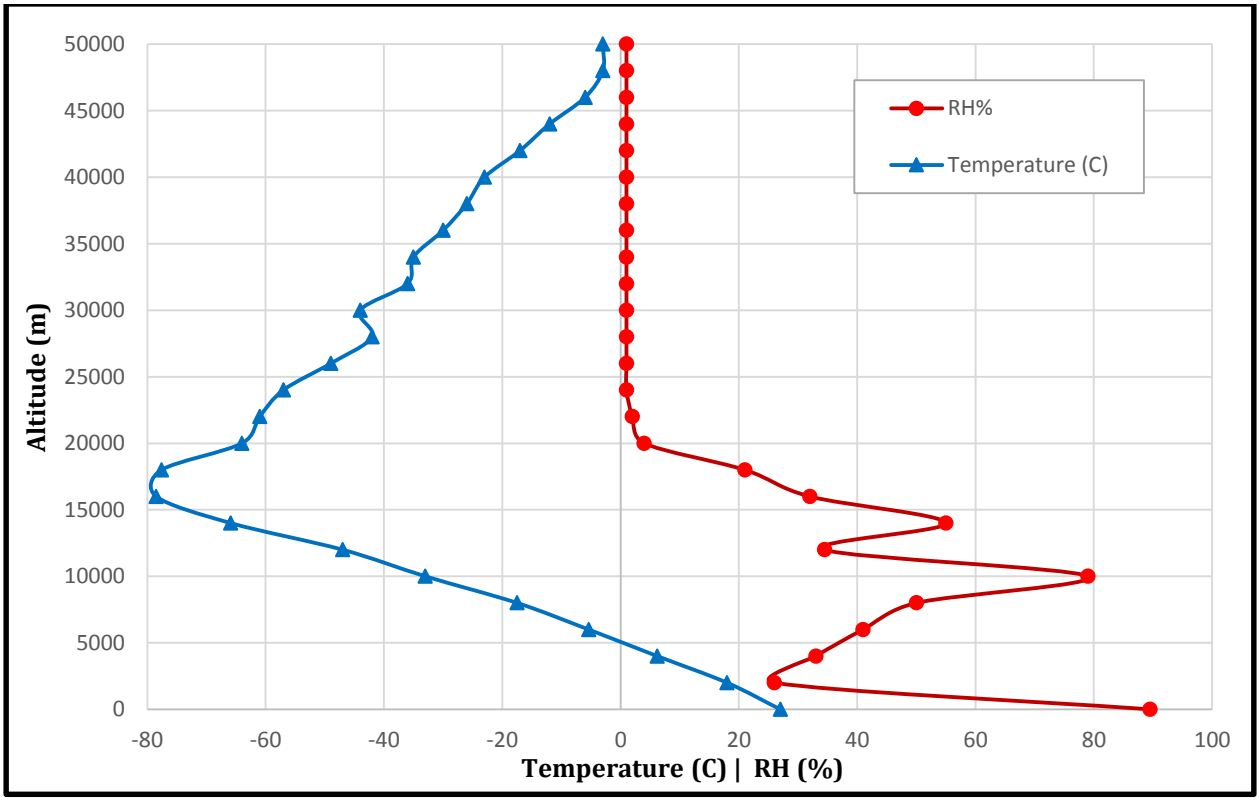

Figure 10: A plot of temperature and relative humidity used for the warm and wet atmospheric profile. Atmospheric data was retrieved from the Piarco International Airport, Trinidad and Tobago radiosonde station. Station latitude is 10.58 degrees; longitude is -61.35 degrees. Data shown is a monthly average of June 2015. Climate for this area is maritime tropical with an annual mean temperature of 26 degrees C.

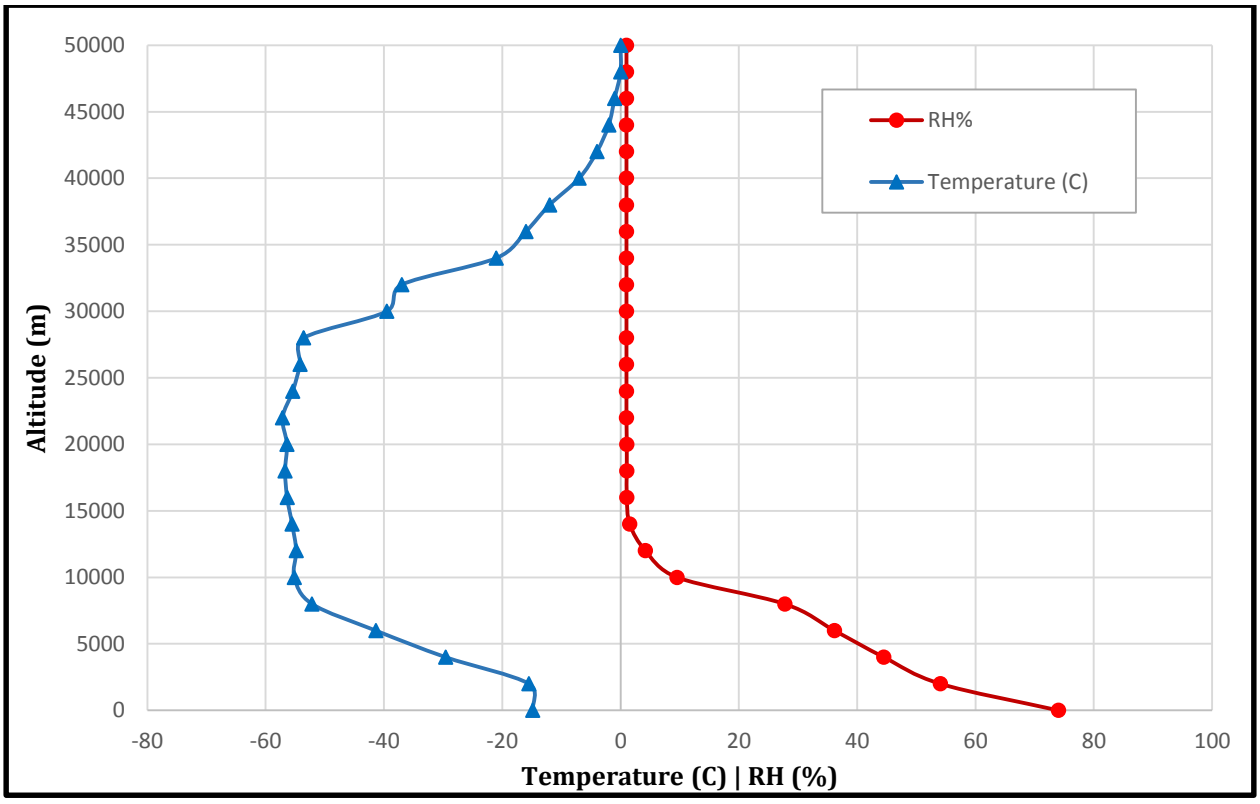

Figure 11: A plot of temperature and relative humidity used for the cold and dry atmospheric profile. Atmospheric data was retrieved from Inuvik, Canada radiosonde station. Station latitude is 68.31 degrees; longitude is -133.53 degrees. Data shown is a monthly average of February 2015. Climate of Inuvik is subarctic with an average annual temperature of -8.2 degrees C and an average February temperature of -25.5 degrees C.

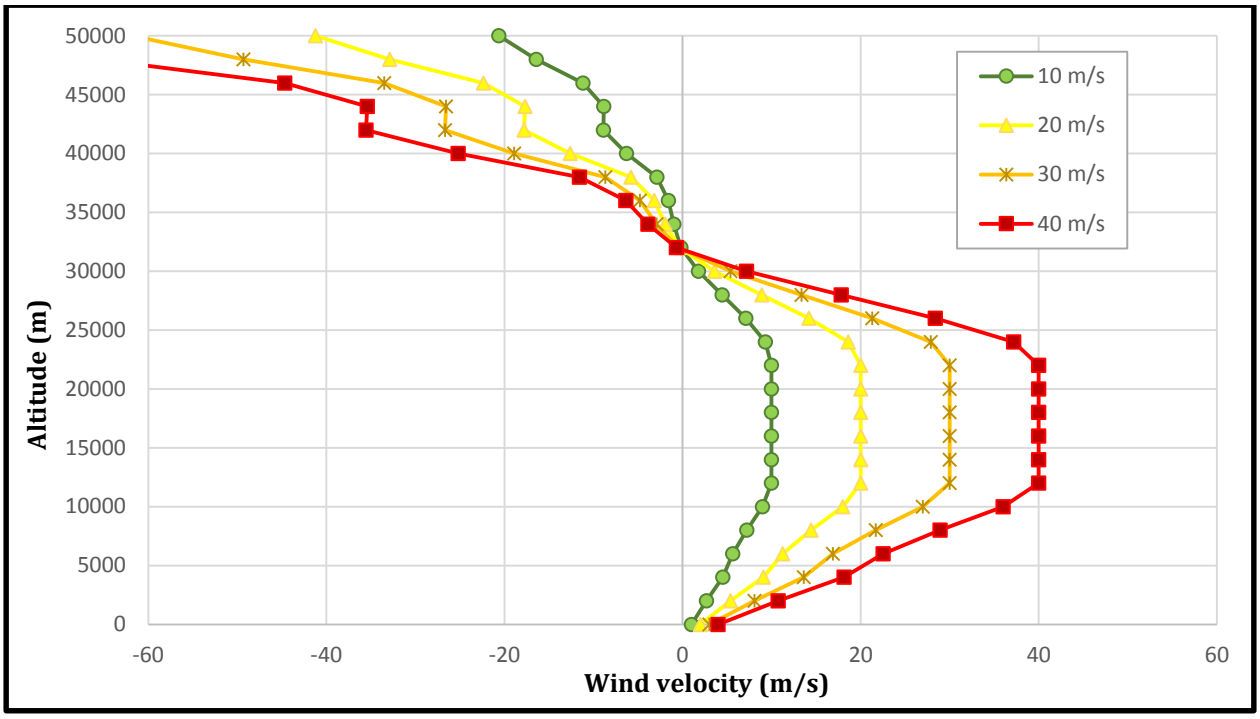

Figure 12: A graph of wind profiles used in the with-wind simulations. Each wind profile is defined here by the maximum wind velocity aloft (i.e. 10, 20, 30, and 40 m/s). The 10 m/s wind profile is the base profile from which the others are scaled to match the desired maximum temperature. This maximum wind velocity range, between 0 and 40 m/s, is chosen in order to encapsulate a wide range of potential wind velocity scenarios and to closely match other wind velocity profiles used in previous works, e.g., Carey and Sparks (1986).

Simulations were run in either a no-wind cylindrical coordinate system (for 2D) or a Cartesian coordinate system (for 3D). The 2D grid was set to 130 grid points in the horizontal (x) direction and 139 grid points in the vertical (z) direction while in 3D the y-direction was also set to 130 grid points. The total x domain was set to 100 km and the y-direction to 50 km. The height of the volcano was arbitrarily set to 1600 m asl. with a crater depth of 50 m. The solution grid in 3D was initialized to 130x130x139 (x, y, z directions) with domain sizes of 100 km^2 area on ground level to an altitude of 50 km. Due to grid scaling, the space between grid points varies between 30 m at the vent to 843 m at the edge of simulation space. Each simulation was set to model the sustained eruption for 60 minutes. Simulations in

3D were run with MPI parallelism with work divided across 81 processors (9 in both x and y directions) on the Falcon supercomputer housed at Idaho National Laboratory. This number of processors provided a relatively quick turnaround from start to finish while not consuming too many resources from the shared supercomputer. Runtimes for each simulation with this setup ranged between 30 and 75 hours, depending on vent exit velocity used, where higher vent velocities lead to increased runtimes.

3.4.1: Defining Stability

There are three plume stability states used in this work, defined here: fully stable, partially unstable, and fully unstable. Fully stable plumes are defined as a buoyant plume with little to no PDC generation. Partially unstable plumes are buoyant plumes with a significant portion of material producing PDCs. Finally, a fully unstable eruption is characterized by PDC generation from complete plume collapse; these may look like material boiling over from the crater. Fine ash elutriates from the tops of PDCs to form phoenix clouds or co-ignimbrites; since these buoyant plumes originate from the PDC rather than directly from the vent, these are consistent with the fully unstable definition. We classify plume stability based on visual inspection of the output imagery and ash concentration along a vertical profile 1 km beyond the edge of the vent in the x-direction. To further constrain plume stability in partially-stable situations, we record the number of minutes after the onset of the eruption at which a plume first destabilizes to produce PDCs.

3.4.2: Observing Simulations

ATHAM-generated netCDF output files were visualized with the UNIDATA IDV software (Meertens et al., 2004) using the UNAVCO IDV plugin (Meertens and Wier, 2007). The plume surface is displayed via an isosurface contour filter set for a concentration of 0.05 g/kg ash. The 12.5 μm ash tracer was used as the medium for visualization. In nature, plume edges are abrupt; in numerical simulations, however, the edges of a plume are blurred as a result of numerical algorithms. As such, we must select a representative isosurface concentration to use as the visible plume edge. We chose the isosurface value of 0.05 g/kg ash concentration, because it generally created continuous surfaces without resulting in excessive smoothing of plume morphology or holes in the plume surface. The maximum plume height is measured from the top of the upper neutral buoyancy zone in the no-wind case. For with-wind simulations, the maximum plume height was measured from the upper extent of the down-wind plume.

Table 1: A tabled list of all simulations completed in 3D under the warm and wet atmospheric profile.

Vent Ejection Velocity (m/s)	Vent Size (m)	Wind Profile
100	100	No Wind
100	1000	No Wind
100	3000	No Wind
200	100	No Wind
200	1000	No Wind
200	3000	No Wind
300	100	No Wind
300	1000	No Wind
300	3000	No Wind
400	100	No Wind
400	1000	No Wind
400	3000	No Wind
100	100	10 m/s
100	1000	10 m/s
100	3000	10 m/s
200	100	10 m/s
200	1000	10 m/s
200	3000	10 m/s
300	100	10 m/s
300	1000	10 m/s
300	3000	10 m/s
400	100	10 m/s
400	1000	10 m/s
400	3000	10 m/s
100	100	20 m/s
100	1000	20 m/s
100	3000	20 m/s
200	100	20 m/s
200	1000	20 m/s
200	3000	20 m/s
300	100	20 m/s
300	1000	20 m/s
300	3000	20 m/s
400	100	20 m/s
400	1000	20 m/s
400	3000	20 m/s
100	100	30 m/s
100	1000	30 m/s
100	3000	30 m/s
200	100	30 m/s
200	1000	30 m/s
200	3000	30 m/s
300	100	30 m/s

300	1000	30 m/s
300	3000	30 m/s
400	100	30 m/s
400	1000	30 m/s
400	3000	30 m/s
100	100	40 m/s
100	1000	40 m/s
100	3000	40 m/s
200	100	40 m/s
200	1000	40 m/s
200	3000	40 m/s
300	100	40 m/s
300	1000	40 m/s
300	3000	40 m/s
400	100	40 m/s
400	1000	40 m/s
400	3000	40 m/s

Table 2: A tabled list of all simulations completed in 3D under the cold and dry atmospheric profile.

Vent Ejection Velocity (m/s)	Vent Size (m)	Wind Profile
100	100	No Wind
100	1000	No Wind
100	3000	No Wind
200	100	No Wind
200	1000	No Wind
200	3000	No Wind
300	100	No Wind
300	1000	No Wind
300	3000	No Wind
400	100	No Wind
400	1000	No Wind
400	3000	No Wind
100	100	10 m/s
100	1000	10 m/s
100	3000	10 m/s
200	100	10 m/s
200	1000	10 m/s
200	3000	10 m/s
300	100	10 m/s
300	1000	10 m/s
300	3000	10 m/s
400	100	10 m/s
400	1000	10 m/s
400	3000	10 m/s
100	100	20 m/s
100	1000	20 m/s
100	3000	20 m/s
200	100	20 m/s
200	1000	20 m/s
200	3000	20 m/s
300	100	20 m/s
300	1000	20 m/s
300	3000	20 m/s
400	100	20 m/s
400	1000	20 m/s
400	3000	20 m/s
100	100	30 m/s
100	1000	30 m/s
100	3000	30 m/s
200	100	30 m/s
200	1000	30 m/s
200	3000	30 m/s
300	100	30 m/s
300	1000	30 m/s

300	3000	30 m/s
400	100	30 m/s
400	1000	30 m/s
400	3000	30 m/s
100	100	40 m/s
100	1000	40 m/s
100	3000	40 m/s
200	100	40 m/s
200	1000	40 m/s
200	3000	40 m/s
300	100	40 m/s
300	1000	40 m/s
300	3000	40 m/s
400	100	40 m/s
400	1000	40 m/s
400	3000	40 m/s

Table 3: A tabled list of all simulations completed in 2D under the warm and wet atmospheric profile.

Vent Ejection Velocity (m/s)	Vent Size (m)	Wind Profile
100	100	No Wind
200	1000	No Wind
400	3000	No Wind

Table 4: A tabled list of all simulations completed in 2D under the cold and dry atmospheric profile.

Vent Ejection Velocity (m/s)	Vent Size (m)	Wind Profile
100	100	No Wind
200	1000	No Wind
400	3000	No Wind

3.5: Results

Over 150 ATHAM simulations were used to examine atmospheric impacts as well as initial vent conditions on column stability. Completed simulations are listed in Tables 1-4, including inputs and stability type. Figures 13, 14, and 15 show output in the cold-dry atmospheric profile while figures 16, 17, and 18 show output from eruptions in the warm-wet atmosphere. The eruptions in Figures 13 and 16 are defined as partially unstable due to continuous PDCs from the start of the eruption coupled with a well-defined buoyant plume. Figures 14 and 17 exemplify the defined fully unstable type due to its lack of a strong vertical rise component; they instead show a prominent lateral translation with-wind and ground-hugging PDCs. Finally, figures 15 and 18 show examples of initially stable eruptions, where the initial stages of the eruption produce a stable plume with no PDCs followed by destabilization of the plume and subsequent collapse and generation of PDCs mid-eruption. The timing of PDC occurrence on the ground is recorded in these initially stable eruptions. In the warm-wet atmosphere, 19% of eruptions were categorized as partially unstable, 26% as fully unstable, and 47% as initially stable. Comparatively, the cold-dry atmosphere had 15% of eruptions categorized as partially unstable, 20% as fully unstable, and 65% as initially stable. Thus, more eruptions were categorized as unstable in the warm-wet atmosphere while the cold-dry atmosphere had more initially stable plumes.

The no-wind eruptions with the largest vent velocities considered here were initially stable before collapsing to form extensive PDCs after reaching maximum plume heights of ~25 km in the warm-wet atmosphere (Fig. 19) and ~17.5 km in

the cold-dry atmosphere (Fig. 20). In 3D, maximum plume heights in the warm-wet atmosphere average ~1.3x higher than their cold-dry counterpart. However, PDC collapse times in the cold-dry atmosphere were an average of ~1.5x minutes later than in the warm-wet atmosphere. Comparing plots of MER and maximum plume height (Figs. 19 & 20) show four clusters of eruptions. Each cluster represents one of the vent diameters used in this study (i.e., 100, 250, 1000, 3000 m) with larger vent diameters representing the greatest MERs. Eruptions in the warm-wet atmosphere show a greater spread of column heights within each cluster than those erupted into the cold-dry atmosphere (Figs. 21 & 22).

Comparing 2D and 3D output shows that only 1 set of simulations differ in their stability classification. However, the elapsed time between eruption start and PDC initiation is longer for 2D by 8 to 21 minutes for otherwise identical eruptions. While maximum plume heights are consistent between 2D and 3D (Tables 5-8), the known limitations of 2D approaches on entrainment calculation (Suzuki et al., 2005; Ogden et al., 2008; Ongaro et al., 2008; Costa et al., 2016) result in later collapse. Thus, we suggest caution when considering the use of ATHAM 2D to determine plume stability.

3.5.1: Wind Effects

Eruptions classified as partially unstable only exist under no-wind or 10 m/s peak wind velocity conditions and at vent exit velocities of 100 and 200 m/s (Figs. 23 & 24). At higher wind velocities, they transition to fully unstable as the plume curves downwind and continuously produces PDCs throughout the eruption.

Conversely, increasing the vent exit velocity over 200 m/s transitions the plume to the initially stable classification in all wind velocity profiles, where PDCs are generated mid-eruption. We found that increasing the vent diameter alone for initially stable plumes resulted in PDCs occurring later in the eruption for all wind velocities (Fig. 25), indicating that larger vent sizes may have a stabilizing effect; this is counter to expectations, since the difference in increase in plume circumference vs. area should act to choke entrainment. Comparing eruptions in no-wind to those in the 40 m/s wind profile shows that maximum plume heights are ~1.4x higher in no-wind for both atmospheric profiles. Furthermore, comparing PDC lateral extent from select output in no-wind and in 20 m/s wind (refer to Figs. 13 & 14, and 16 & 17) show PDC extents with-wind extend to a greater maximum distance by about 4 km. PDC extension is driven in primarily the with-wind direction, leaving the remaining area around the volcano with less PDC activity, although PDCs can still extend for multiple km in other directions (Figs. 14 & 17).

3.5.2: Tropopause

We examined the importance of tropopause height relative to atmospheric temperature and relative humidity by rescaling the warm-wet and cold-dry profiles for the opposite tropopause heights. Output from the down-scaled warm atmosphere exhibited a form of total umbrella collapse (Fig. 26) that was not seen in any other output, indicating that the increased lapse rate in ambient temperature and relative humidity as well as the lower tropopause height can lead to a complete destabilization of the umbrella cloud. Plume height observations show most eruptions with vent exit velocities at or exceeding 200 m/s in both atmospheres

were able to breach the tropopause and enter the stratosphere in all wind velocity profiles. Specifically, 70% of eruptions in the warm-wet atmosphere breached the tropopause, while the cold-dry atmosphere breached 60% of the time. The remaining eruptions had either a low vent exit velocity (100 m/s) or a high wind velocity profile that prevented the necessary vertical rise to puncture the tropopause.

Table 5: A tabled list of all simulations completed in 2D under the warm and wet atmospheric profile. Stability Type is one of three categories: 1) Fully Unstable, 2) Partially Unstable, 3) Initially Stable, then Unstable.

Vent Ejection Velocity (m/s)	Vent Size (m)	Wind Profile	MER (kg/s)	Max Height (km)	PDC Time (minutes)	Stability Type
100	100	No Wind	9.42E+06	20	1.5	2
200	1000	No Wind	1.88E+09	20	18	3
400	3000	No Wind	3.39E+10	25	48	3

Table 6: A tabled list of all simulations completed in 2D under the cold and dry atmospheric profile. Stability Type is one of three categories: 1) Fully Unstable, 2) Partially Unstable, 3) Initially Stable, then Unstable.

Vent Ejection Velocity (m/s)	Vent Size (m)	Wind Profile	MER (kg/s)	Max Height (km)	PDC Time (minutes)	Stability Type
100	100	No Wind	9.42E+06	12	1.5	2
200	1000	No Wind	1.88E+09	16	45	3
400	3000	No Wind	3.39E+10	17	54	3

Table 7: A tabled list of all simulations completed in 3D under the warm and wet atmospheric profile. Stability Type is one of three categories: 1) Fully Unstable, 2) Partially Unstable, 3) Initially Stable, then Unstable.

Vent Ejection Velocity (m/s)	Vent Size (m)	Wind Profile	MER (kg/s)	Max Height (km)	PDC Time (minutes)	Stability Type
100	100	No Wind	9.42E+06	17.5	1.5	2
100	1000	No Wind	9.42E+08	17.5	1.5	2
100	3000	No Wind	8.48E+09	18	1.5	2
200	100	No Wind	1.88E+07	18.5	1.5	2
200	1000	No Wind	1.88E+09	18.5	1.5	2
200	3000	No Wind	1.70E+10	19.5	1.5	2
300	100	No Wind	2.83E+07	20	12	3
300	1000	No Wind	2.83E+09	22	21	3
300	3000	No Wind	2.54E+10	22.5	22.5	3
400	100	No Wind	3.77E+07	25	28.5	3
400	1000	No Wind	3.77E+09	25	36	3
400	3000	No Wind	3.39E+10	25	37.5	3
100	100	10 m/s	9.42E+06	15	1.5	2
100	1000	10 m/s	9.42E+08	16.5	1.5	2
100	3000	10 m/s	8.48E+09	17	1.5	2
200	100	10 m/s	1.88E+07	21	1.5	2
200	1000	10 m/s	1.88E+09	20	1.5	2
200	3000	10 m/s	1.70E+10	19	1.5	2
300	100	10 m/s	2.83E+07	22	7.5	3
300	1000	10 m/s	2.83E+09	20	21	3
300	3000	10 m/s	2.54E+10	21	21	3
400	100	10 m/s	3.77E+07	24	21	3
400	1000	10 m/s	3.77E+09	23.5	34.5	3
400	3000	10 m/s	3.39E+10	22.5	36	3
100	100	15 m/s	9.42E+06	15	1.5	1
400	100	15 m/s	3.77E+07	20	22.5	3
100	250	15 m/s	5.89E+07	15	1.5	1
200	250	15 m/s	1.18E+08	17.5	1.5	1
300	250	15 m/s	1.77E+08	19	4.5	3
400	250	15 m/s	2.36E+08	19.5	27	3
100	1000	15 m/s	9.42E+08	15.5	1.5	1
200	1000	15 m/s	1.88E+09	17.5	1.5	1
300	1000	15 m/s	2.83E+09	17.5	19.5	3
100	3000	15 m/s	8.48E+09	15	1.5	1
400	3000	15 m/s	3.39E+10	20	36	3
100	100	20 m/s	9.42E+06	8	1.5	1
100	1000	20 m/s	9.42E+08	7.5	1.5	1
100	3000	20 m/s	8.48E+09	6.5	1.5	1
200	100	20 m/s	1.88E+07	17.5	1.5	1
200	1000	20 m/s	1.88E+09	18	1.5	1
200	3000	20 m/s	1.70E+10	17.5	1.5	1

300	100	20 m/s	2.83E+07	19	3	3
300	1000	20 m/s	2.83E+09	19.5	19.5	3
300	3000	20 m/s	2.54E+10	19.5	21	3
400	100	20 m/s	3.77E+07	20	25.5	3
400	1000	20 m/s	3.77E+09	20.5	31.5	3
400	3000	20 m/s	3.39E+10	19.5	36	3
100	100	30 m/s	9.42E+06	8	1.5	1
100	1000	30 m/s	9.42E+08	7	1.5	1
100	3000	30 m/s	8.48E+09	7.5	1.5	1
200	100	30 m/s	1.88E+07	17	1.5	1
200	1000	30 m/s	1.88E+09	16.5	1.5	1
200	3000	30 m/s	1.70E+10	16.5	1.5	1
300	100	30 m/s	2.83E+07	17	1.5	1
300	1000	30 m/s	2.83E+09	17.5	21	3
300	3000	30 m/s	2.54E+10	17	21	3
400	100	30 m/s	3.77E+07	18	27	3
400	1000	30 m/s	3.77E+09	18.5	33	3
400	3000	30 m/s	3.39E+10	18.5	33	3
100	100	40 m/s	9.42E+06	9	1.5	1
100	1000	40 m/s	9.42E+08	7	1.5	1
100	3000	40 m/s	8.48E+09	8	1.5	1
200	100	40 m/s	1.88E+07	14	1.5	1
200	1000	40 m/s	1.88E+09	13	1.5	1
200	3000	40 m/s	1.70E+10	12	1.5	1
300	100	40 m/s	2.83E+07	18	1.5	1
300	1000	40 m/s	2.83E+09	14	30	3
300	3000	40 m/s	2.54E+10	14	27	3
400	100	40 m/s	3.77E+07	17	31.5	3
400	1000	40 m/s	3.77E+09	18	37.5	3
400	3000	40 m/s	3.39E+10	18.5	37.5	3

Table 8: A tabled list of all simulations completed in 3D under the cold and dry atmospheric profile. Stability Type is one of three categories: 1) Fully Unstable, 2) Partially Unstable, 3) Initially Stable, then Unstable. 'NA' refers to runs that did not complete successfully.

Vent Ejection Velocity (m/s)	Vent Size (m)	Wind Profile	MER (kg/s)	Max Height (km)	PDC Time (minutes)	Stability Type
100	100	No Wind	9.42E+06	13	1.5	2
100	1000	No Wind	9.42E+08	13	1.5	2
100	3000	No Wind	8.48E+09	12	1.5	2
200	100	No Wind	1.88E+07	15	4.5	3
200	1000	No Wind	1.88E+09	15	24	3
200	3000	No Wind	1.70E+10	14	24	3
300	100	No Wind	2.83E+07	16.5	30	3
300	1000	No Wind	2.83E+09	16	40.5	3
300	3000	No Wind	2.54E+10	15	40.5	3
400	100	No Wind	3.77E+07	17	40.5	3
400	1000	No Wind	3.77E+09	17.5	46.5	3
400	3000	No Wind	3.39E+10	17.5	46.5	3
100	100	10 m/s	9.42E+06	11	1.5	2
100	1000	10 m/s	9.42E+08	10.5	1.5	2
100	3000	10 m/s	8.48E+09	10	1.5	2
200	100	10 m/s	1.88E+07	13.5	1.5	2
200	1000	10 m/s	1.88E+09	12	21	3
200	3000	10 m/s	1.70E+10	13.5	18	3
300	100	10 m/s	2.83E+07	16	30	3
300	1000	10 m/s	2.83E+09	14.5	39	3
300	3000	10 m/s	2.54E+10	15.5	39	3
400	100	10 m/s	3.77E+07	17	39	3
400	1000	10 m/s	3.77E+09	16	45	3
400	3000	10 m/s	3.39E+10	17.5	45	3
100	100	15 m/s	9.42E+06	9	1.5	2
200	100	15 m/s	1.88E+07	11	1.5	2
300	100	15 m/s	2.83E+07	12.5	31.5	3
400	100	15 m/s	3.77E+07	14	40.5	3
100	250	15 m/s	5.89E+07	10	1.5	1
200	250	15 m/s	1.18E+08	12.5	1.5	2
300	250	15 m/s	1.77E+08	13	34.5	3
400	250	15 m/s	2.36E+08	15.5	30+	3
100	1000	15 m/s	9.42E+08	9	1.5	1
200	1000	15 m/s	1.88E+09	11	21	3
400	1000	15 m/s	3.77E+09	16	42	3
100	3000	15 m/s	8.48E+09	9.5	1.5	1
400	3000	15 m/s	3.39E+10	16	46.5	3
100	100	20 m/s	9.42E+06	10	1.5	1
100	1000	20 m/s	9.42E+08	10.5	1.5	1
100	3000	20 m/s	8.48E+09	10.5	1.5	1
200	100	20 m/s	1.88E+07	12	1.5	1

200	1000	20 m/s	1.88E+09	11.5	22.5	3
200	3000	20 m/s	1.70E+10	11	21	3
300	100	20 m/s	2.83E+07	14	28.5	3
300	1000	20 m/s	2.83E+09	12.5	40.5	3
300	3000	20 m/s	2.54E+10	13	39	3
400	100	20 m/s	3.77E+07	14	37.5	3
400	1000	20 m/s	3.77E+09	15	46.5	3
400	3000	20 m/s	3.39E+10	14	45	3
100	100	30 m/s	9.42E+06	9.5	1.5	1
100	1000	30 m/s	9.42E+08	9	1.5	1
100	3000	30 m/s	8.48E+09	9.5	1.5	1
200	100	30 m/s	1.88E+07	10	1.5	1
200	1000	30 m/s	1.88E+09	10.5	19.5	3
200	3000	30 m/s	1.70E+10	11	18	3
300	100	30 m/s	2.83E+07	12.5	30	3
300	1000	30 m/s	2.83E+09	12	39	3
300	3000	30 m/s	2.54E+10	12	37.5	3
400	100	30 m/s	3.77E+07	13.5	40.5	3
400	1000	30 m/s	3.77E+09	14.5	46.5	3
400	3000	30 m/s	3.39E+10	15	46.5	3
100	100	40 m/s	9.42E+06	8.5	1.5	1
100	1000	40 m/s	9.42E+08	8	1.5	1
100	3000	40 m/s	8.48E+09	8	1.5	1
200	100	40 m/s	1.88E+07	9	1.5	1
200	1000	40 m/s	1.88E+09	9	16.5	3
200	3000	40 m/s	1.70E+10	9.5	16.5	3
300	100	40 m/s	2.83E+07	10.5	31.5	3
300	1000	40 m/s	2.83E+09	10	37.5	3
300	3000	40 m/s	2.54E+10	NA	NA	NA (3?)
400	100	40 m/s	3.77E+07	12	39.5	3
400	1000	40 m/s	3.77E+09	NA	NA	NA (3?)
400	3000	40 m/s	3.39E+10	12.5	45.5	3

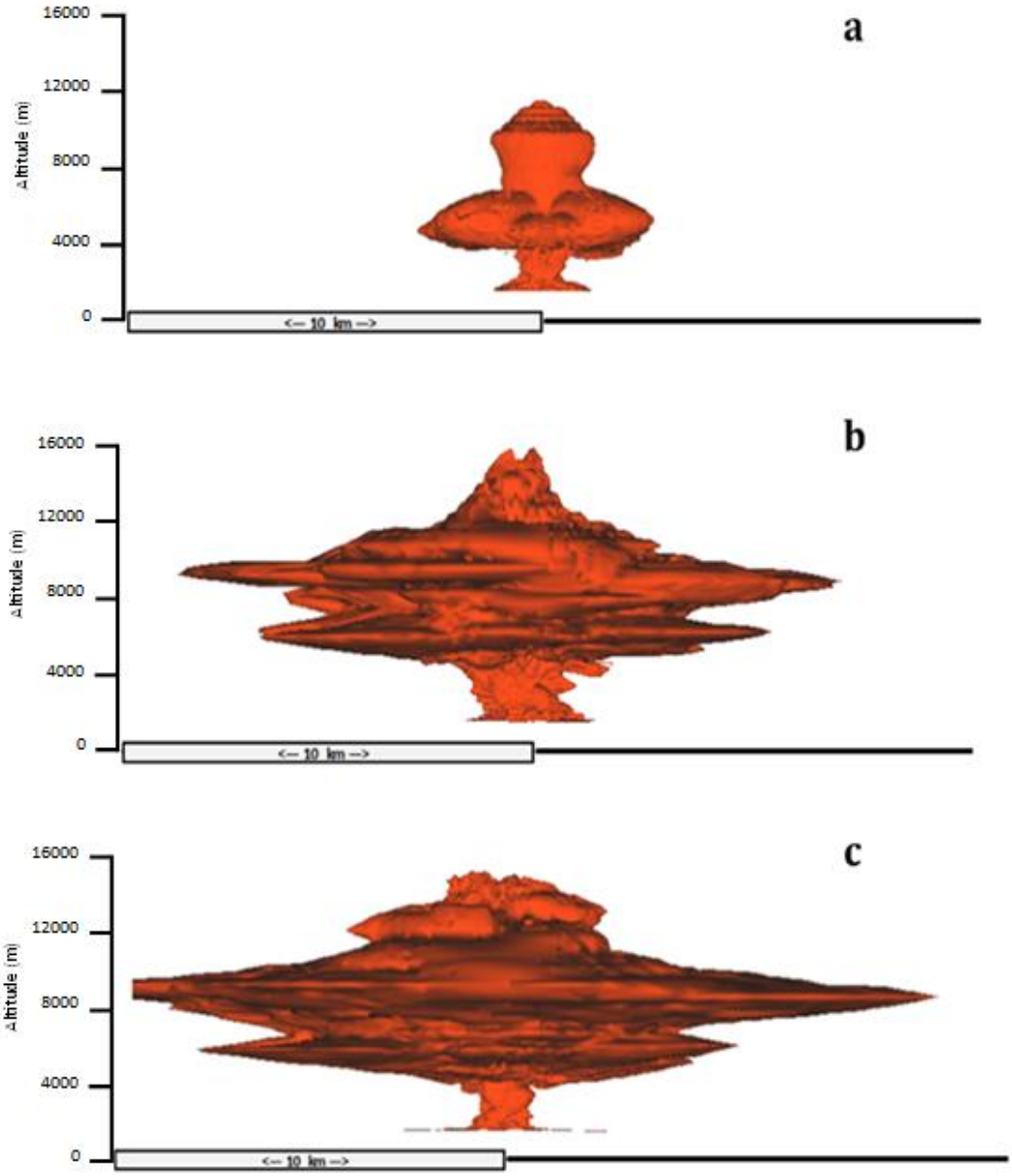

Figure 13: Side view of a 3D eruption in the cold-dry atmospheric profile. Input conditions: 100 m/s vent velocity, 100 m vent size, no-wind. a) 06:00 minutes into eruption, b) 21:00 minutes into eruption, c) 45:00 minutes into eruption. This simulation shows PDC generation at the first time step continuing through the end of the eruption. This, coupled with the high rising plume cloud, categorizes this eruption into the partially unstable type. Most simulations with a low vent exit velocity at 100 or 200 m/s or a low wind velocity up to 15 m/s exhibited a similar plume morphology and PDC generation. The low vent exit velocity does not provide enough momentum for the plume to entrain enough air to reach complete buoyancy before momentum is lost, leading to PDC generation throughout the length of this eruption. PDC extent along the ground for this simulation is ~3 km from the middle of the vent (c). For this and subsequent figures, the volcanic vent is located 1600 m asl.

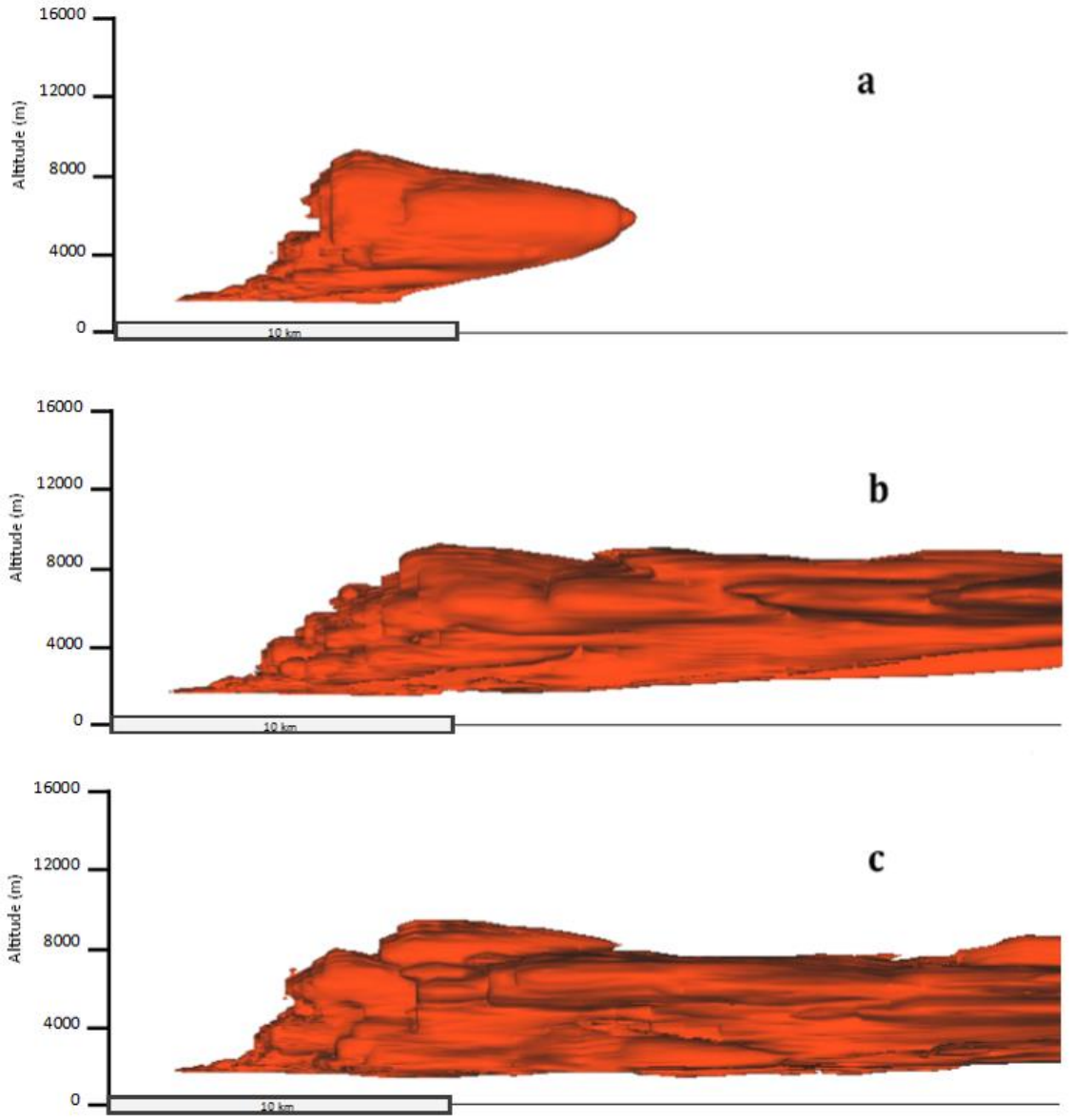

Figure 14: Side view of a 3D eruption in the cold-dry atmospheric profile. Input conditions: 100 m/s vent velocity, 100 m vent size, 40 m/s wind velocity profile. a) 06:00 minutes into eruption, b) 21:00 minutes into eruption, c) 45:00 minutes into eruption. This simulation shows PDC generation at the first time step continuing through the end of the simulation. This, coupled with the strong bending of the plume down-wind, categorizes this eruption into the fully unstable type. Most simulations with a low vent exit velocity at 100 or 200 m/s with a wind velocity profile over 10 m/s exhibited similar plume morphology, specifically plume bending and PDC generation. The 20 m/s wind velocity profile is sufficient to bend the column and significantly reduce maximum column height compared to the no-wind case of the same eruption.

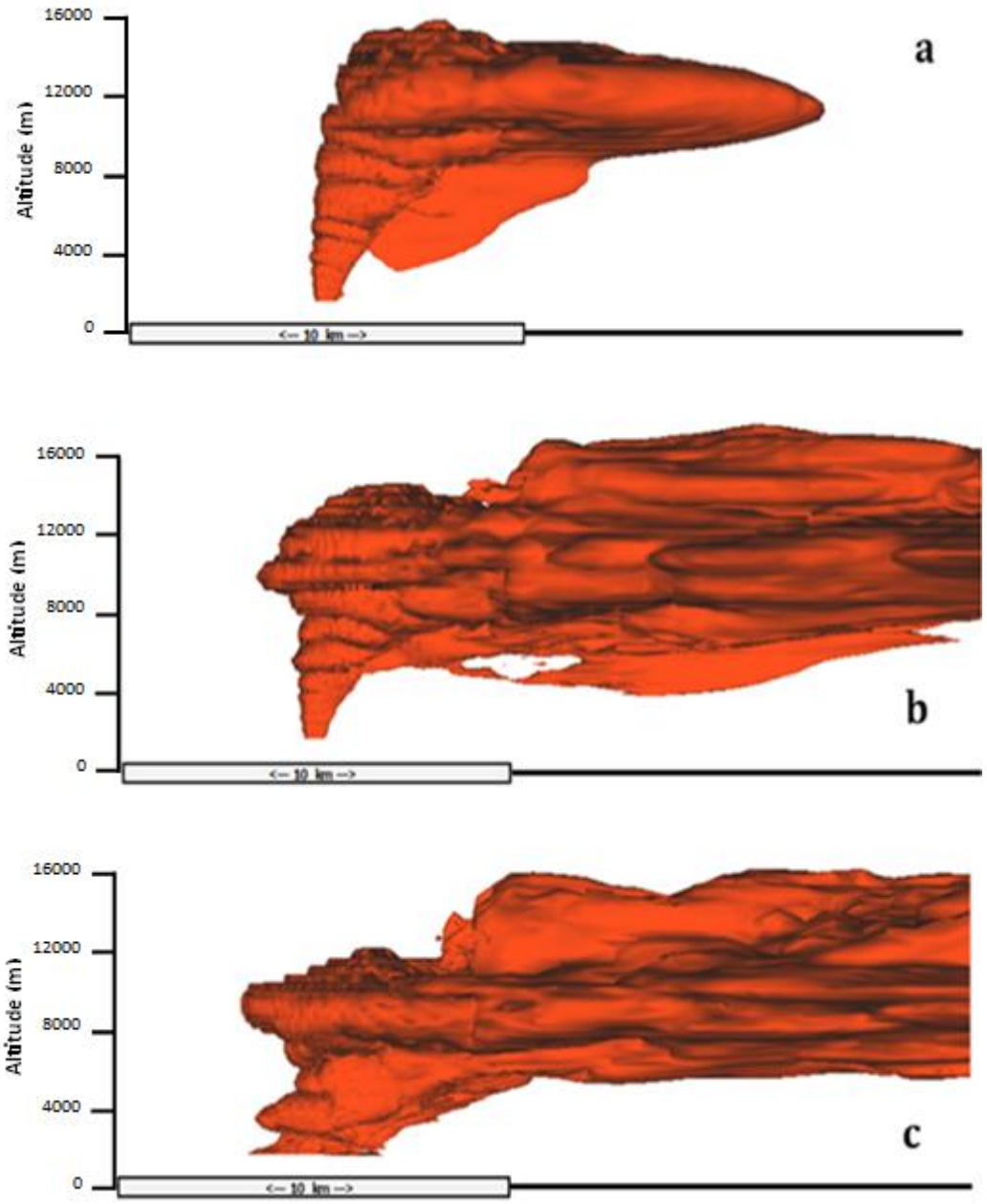

Figure 15: Side view of a 3D eruption in the cold-dry atmospheric profile. Input conditions: 400 m/s vent velocity, 100 m vent size, 20 m/s wind velocity profile. a) 06:00 minutes into eruption, b) 21:00 minutes into eruption, c) 45:00 minutes into eruption. This simulation exhibits a stable plume up until 37.5 minutes into the eruption, when PDCs are shed from the column and continue to do so throughout the remainder of the eruption. This simulation is thus categorized as initially stable. Most simulations with a vent exit velocity above 200 m/s, regardless of wind velocity profile, are categorized as this type.

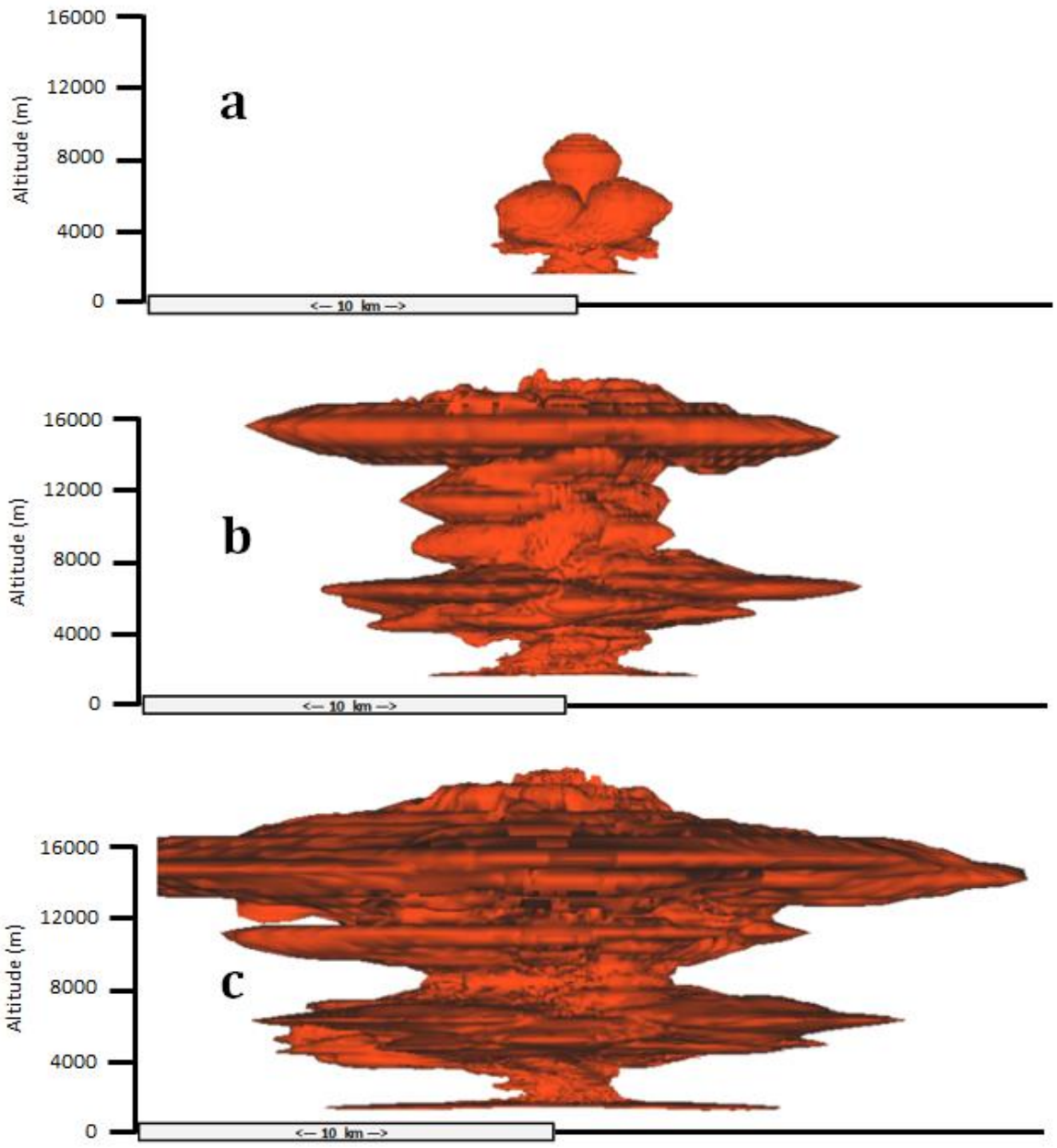

Figure 16*:* Side view of a 3D eruption in the warm-wet atmospheric profile. Input conditions: 100 m/s vent velocity, 100 m vent size, no-wind velocity profile. a) 06:00 minutes into eruption, b) 21:00 minutes into eruption, c) 45:00 minutes into eruption. This simulation shows PDC generation at the first time step continuing through the end of the simulation. This, coupled with the high rising plume cloud, categorizes this eruption into the partially unstable type. PDC extent along the ground for this simulation is ~6 km from the middle of the vent.

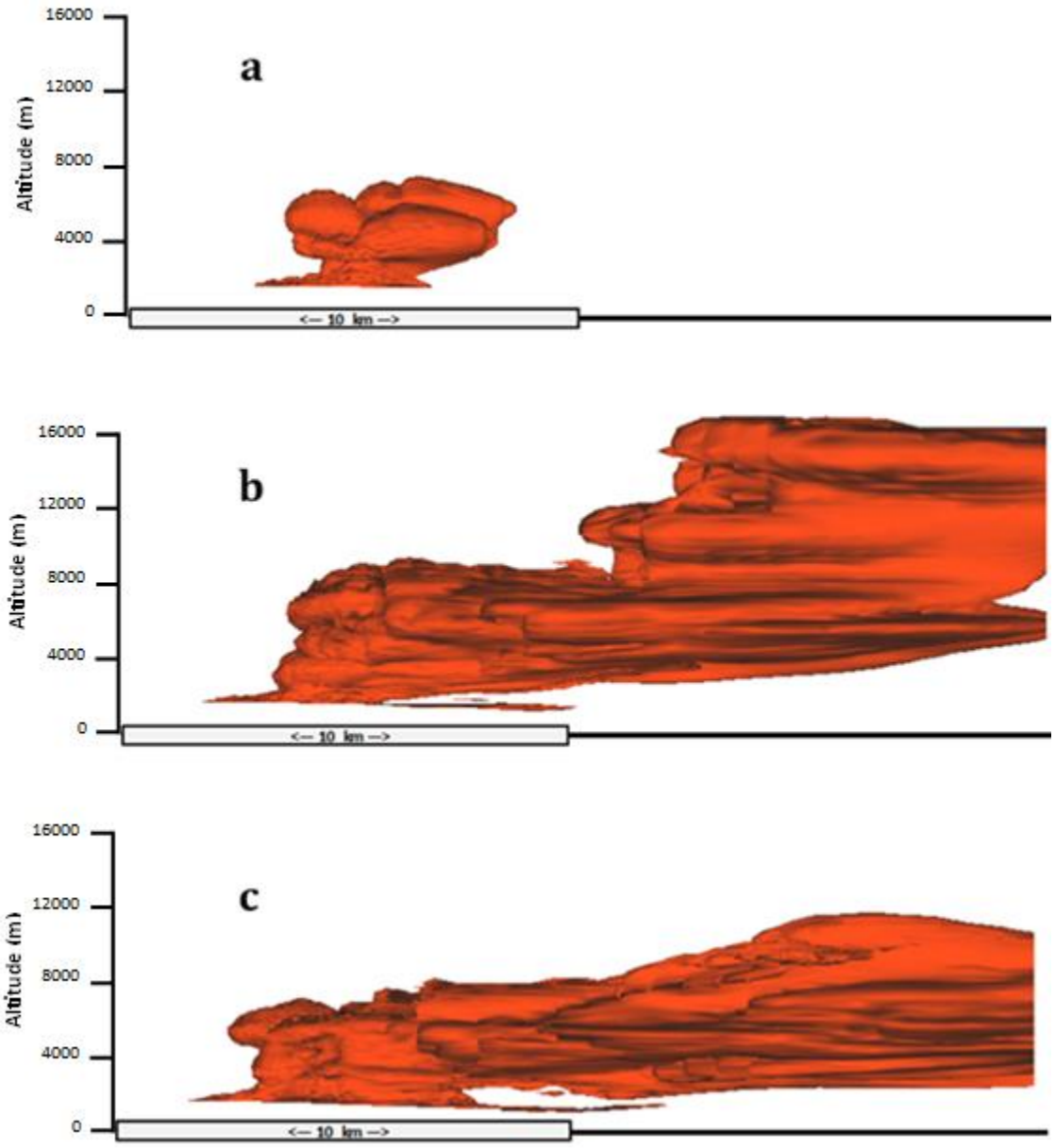

Figure 17: Side view of a 3D eruption in the warm-wet atmospheric profile. Input conditions: 100 m/s vent velocity, 100 m vent size, 20 m/s wind velocity profile. a) 06:00 minutes into eruption, b) 21:00 minutes into eruption, c) 45:00 minutes into eruption. This simulation shows PDC generation at the first time step continuing through the end of the simulation. This, coupled with the strong bending of the plume down-wind, categorizes this eruption into the fully unstable type. PDC extent is about 9 km in the with-wind direction.

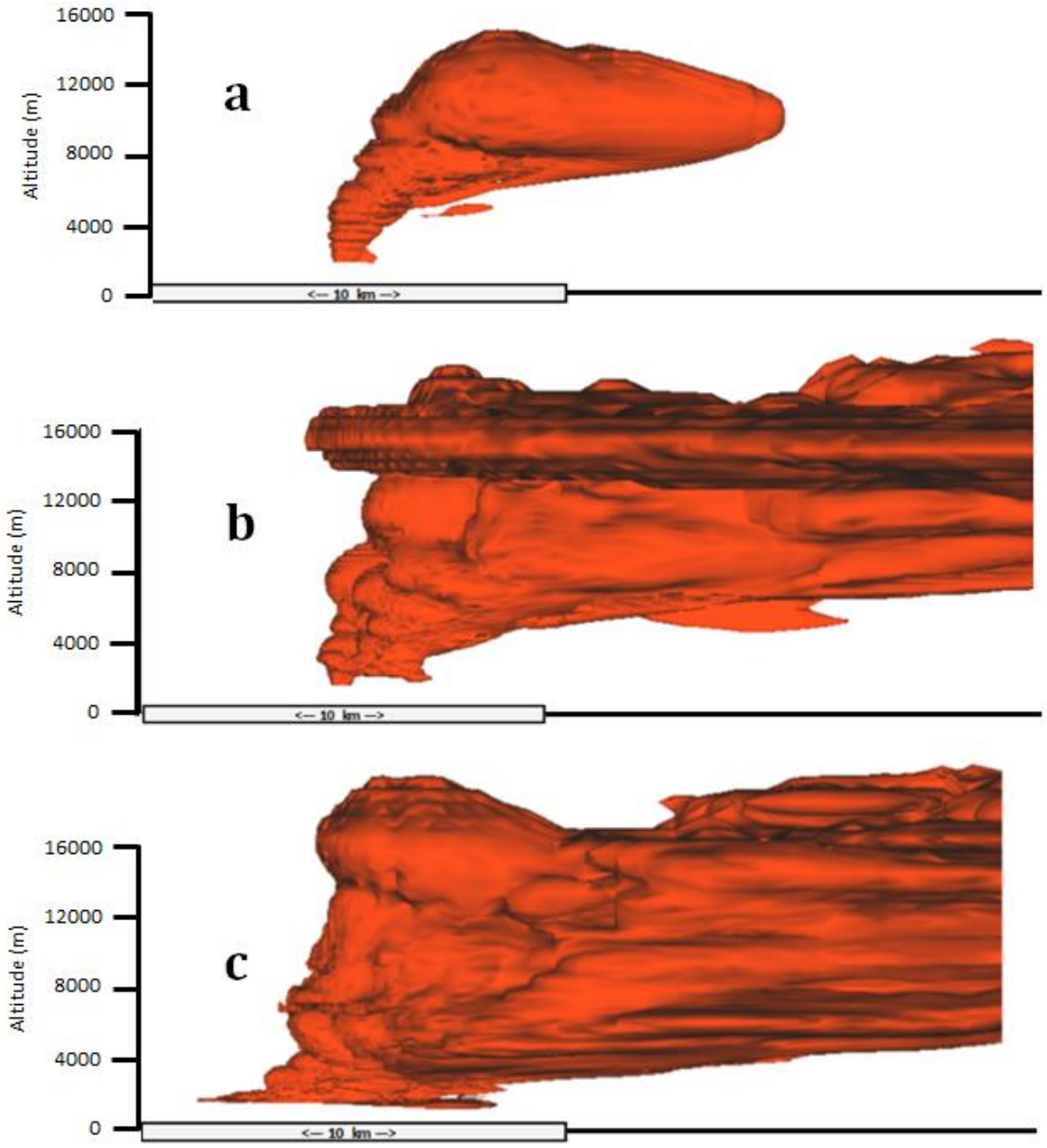

Figure 18: Side view of a 3D eruption in the warm-wet atmospheric profile. Input conditions: 400 m/s vent velocity, 100 m vent size, 20 m/s wind velocity profile. a) 06:00 minutes into eruption, b) 21:00 minutes into eruption, c) 45:00 minutes into eruption. This simulation exhibits a stable plume up until 25.5 minutes into the eruption, when PDCs are shed from the column and continue to do so throughout the remainder of the eruption. This simulation is thus categorized as initially stable.

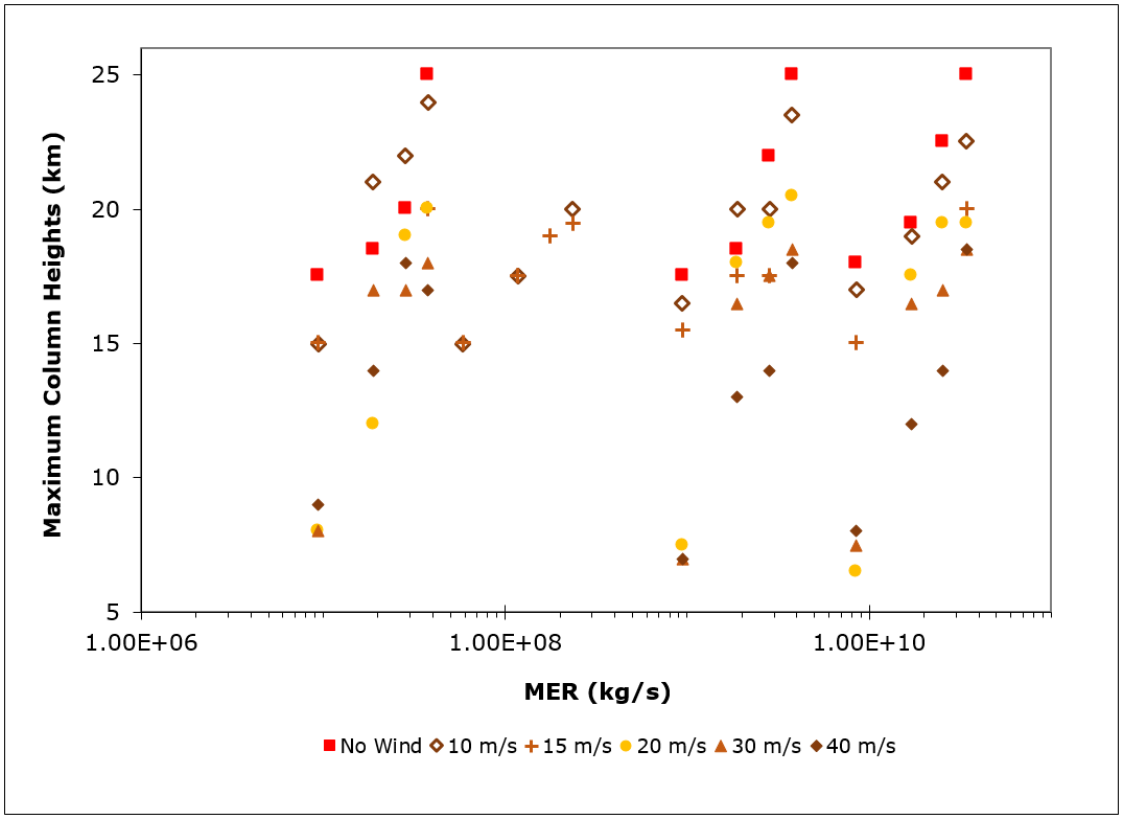

Figure 19: A graph of MER and max column height for the warm-wet atmospheric profile for all wind profiles used. Points below 10 km are where eruptions had a vent exit velocity of 100 m/s and were erupted into a high wind profile (at or above 20 m/s). Three clusters are revealed and are a result of varying vent diameters in the simulations. This indicates that vent diameter has little to no impact on maximum column height. Also shown is a general decrease in column height with wind speed within each cluster.

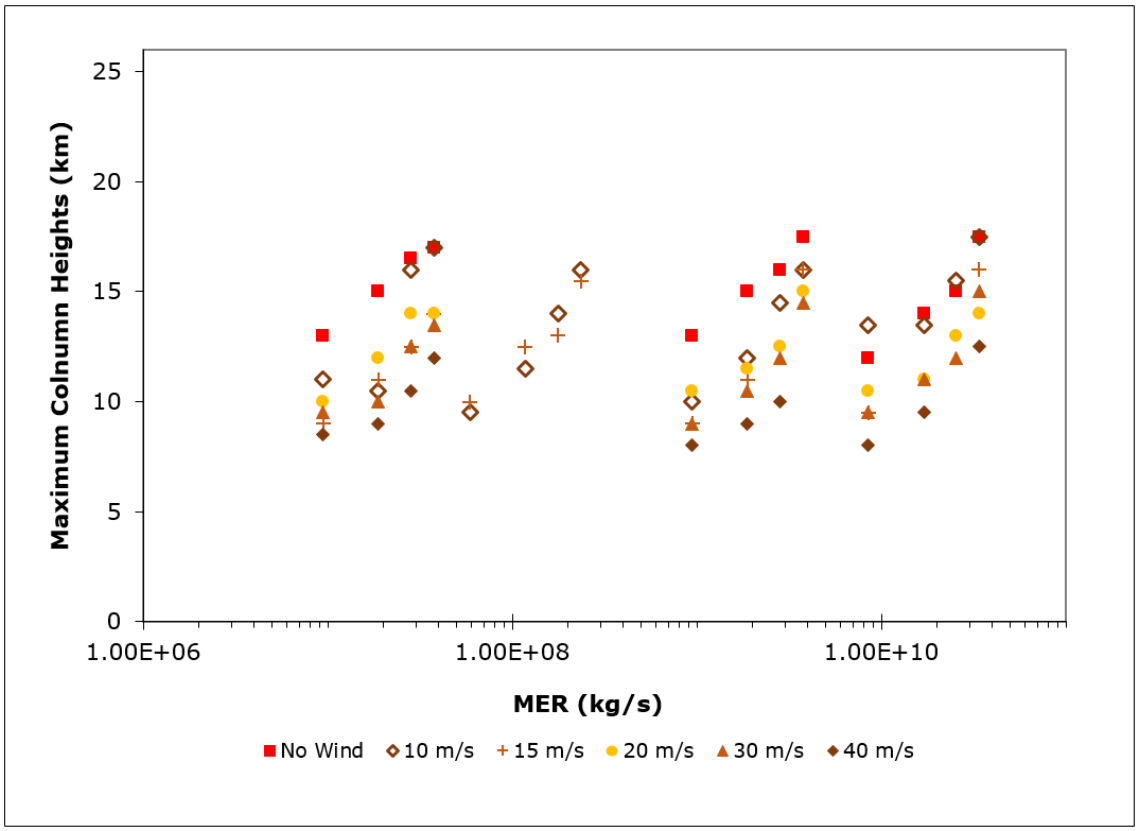

Figure 20: A graph of MER and max column height for the cold-dry atmospheric profile. The points with the lower column heights are also the simulations that had an input vent exit velocity of 100 m/s while the points with the higher column heights had an exit velocity of 400 m/s. The higher points also tend to generate PDCs later in their eruptions than the lower points.

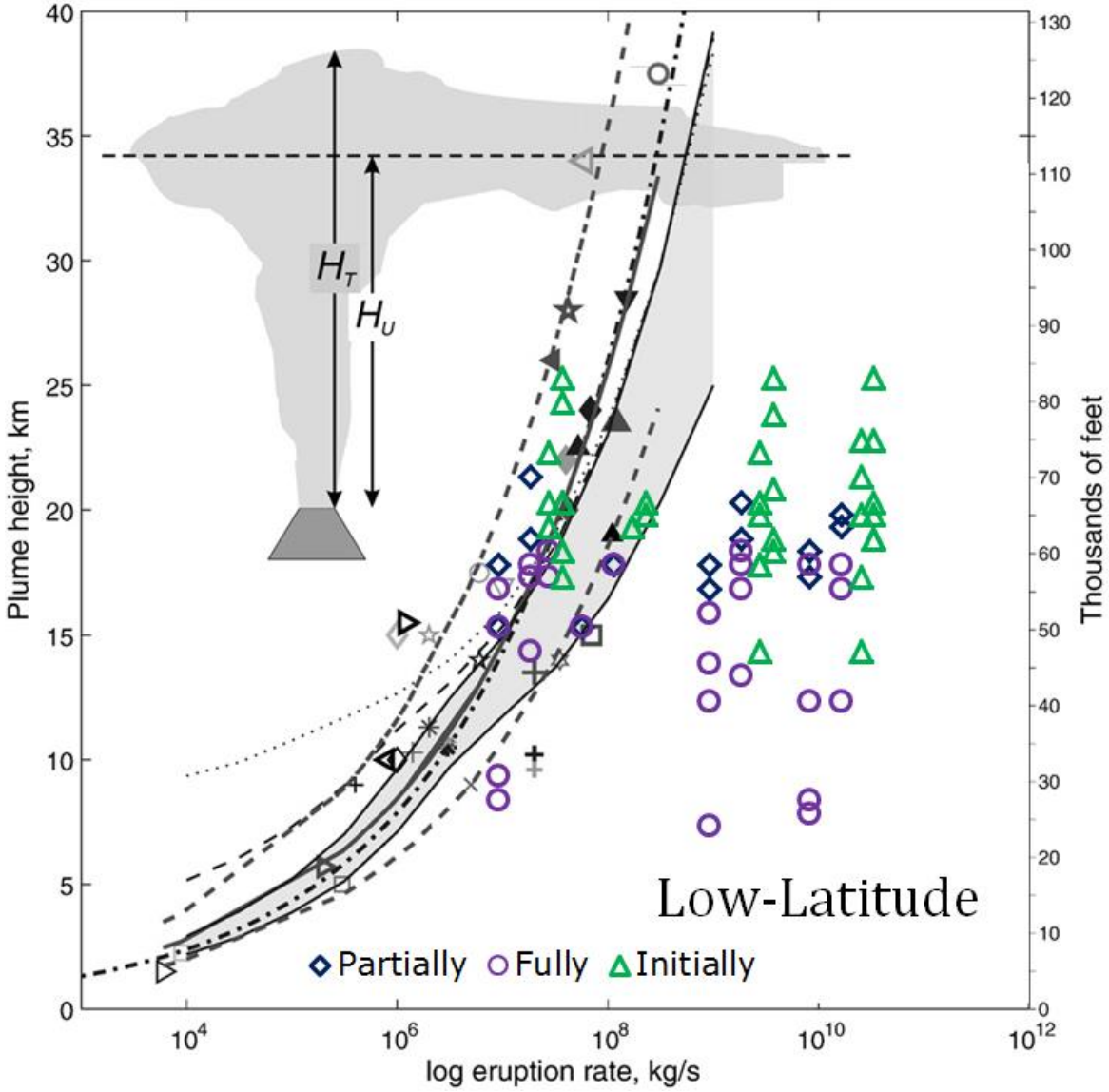

Figure 21: A graph of MER and plume height plotted with real and simulated eruptions. This modified Mastin et al. (2009) figure plots over 30 natural eruptions, identifying an overall best fit. See the original Figure 1 in Mastin et al. (2009) for a list of the plotted eruptions. On top of the original figure is the full suite of eruptions from the cold-dry, low-latitude atmospheric profile categorized by stability type. Plume heights in our simulated eruptions were recorded from the height of the umbrella region (H_u). While the lower MER eruptions plot close to the compiled natural eruptions, the high MER eruptions deviate far to the right. This is likely explained by the relatively sparse occurrence of these large vent size, high MER eruptions in nature.

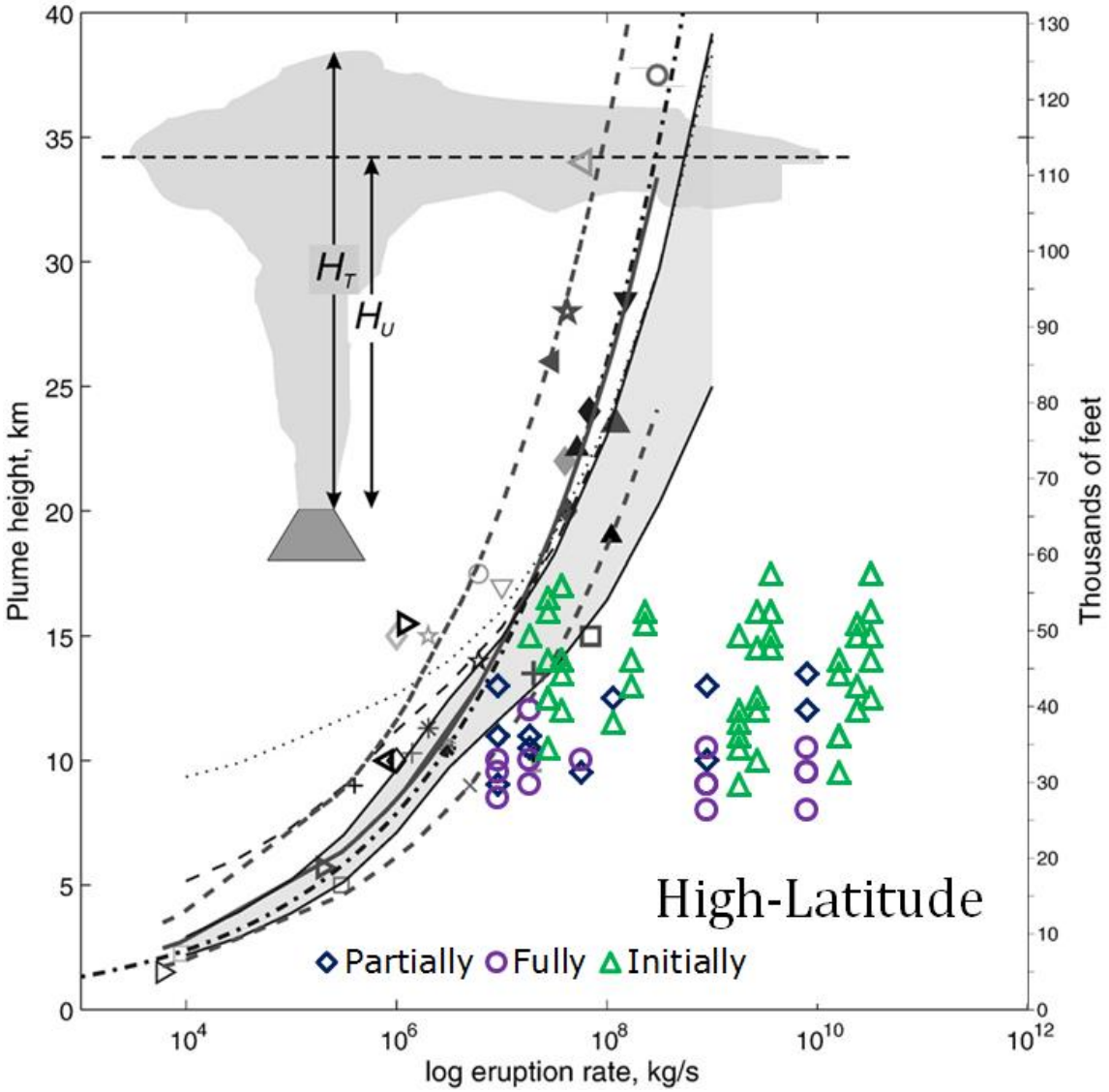

Figure 22: A graph of MER and plume height plotted with real and simulated eruptions. This modified Mastin et al. (2009) figure plots over 30 natural eruptions, identifying an overall best fit. See the original Figure 1 in Mastin et al. (2009) for a list of the plotted eruptions. On top of the original figure is the full suite of eruptions from the warm-wet, high-latitude atmospheric profile categorized by stability type. Plume heights in our simulated eruptions were recorded from the height of the umbrella region (H_u). While the lower MER eruptions plot close to the compiled natural eruptions, the high MER eruptions deviate far to the right. This is likely explained by the relatively sparse occurrence of these large vent size, high MER eruptions in nature.

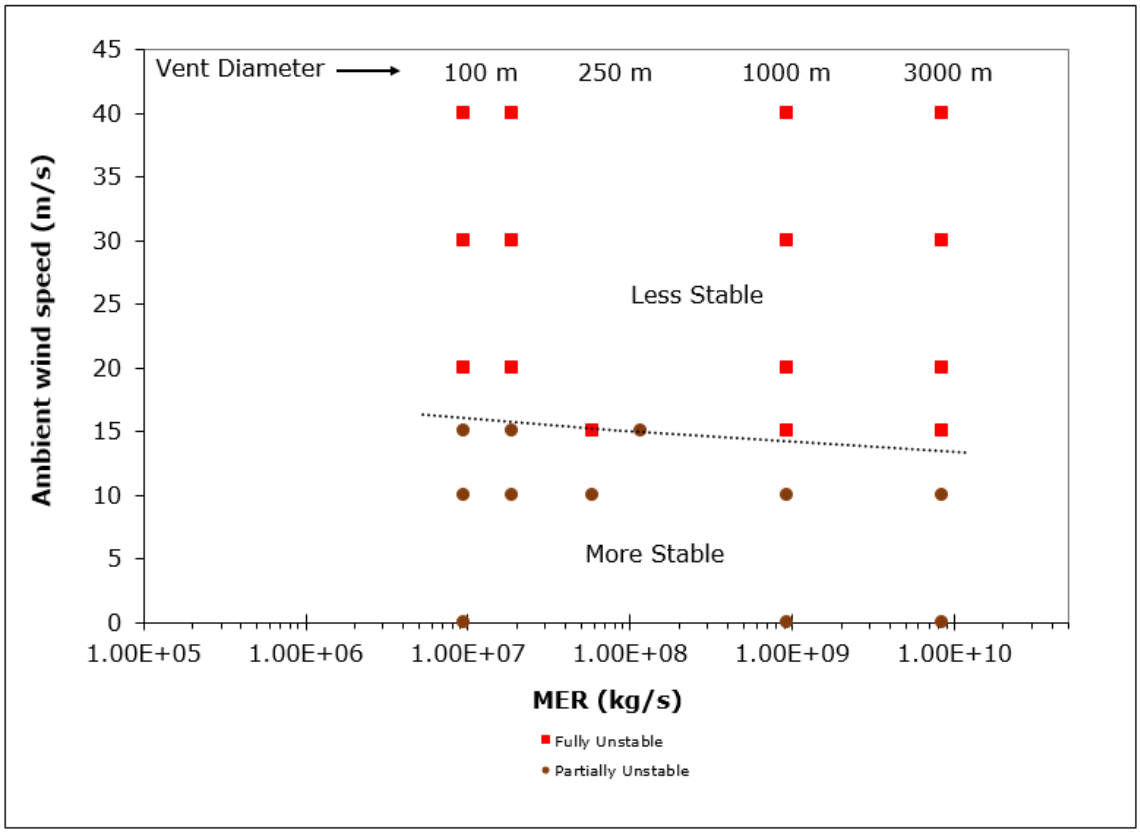

Figure 23: A graph of MER and wind velocity for unstable plumes in the cold-dry atmospheric profile. This plot contains simulations categorized as either partially unstable or fully unstable. Eruptions in these simulations show an apparent increased instability with increasing wind velocities. The plumes in the less stable regime are effectively knocked-over by wind, exhibiting PDC generation throughout the eruption, and this remains true across each vent diameter. For the more stable regime, PDCs are observed throughout the entirety of the eruption. The dotted line represents the approximate transition between the stability regimes. The vent diameter labels indicate the input vent diameters for the eruptions plotted below them.

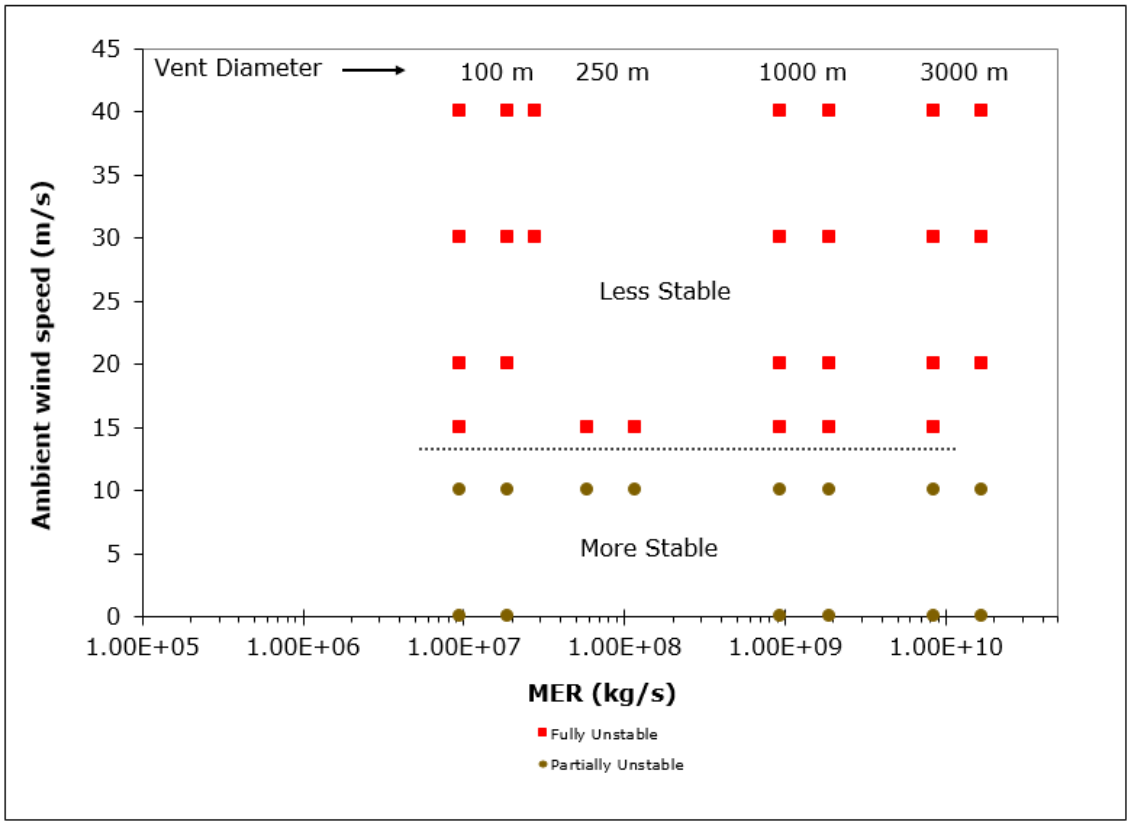

Figure 24: A graph of MER and wind velocity for unstable plumes in the warm-wet atmospheric profile. This plot contains simulations categorized as either partially unstable or fully unstable. Eruptions in these simulations show an apparent increased instability with increasing wind velocities. The plumes in the less stable regime are effectively knocked-over by wind, exhibiting PDC generation throughout the eruption, and this remains approximately true across each vent diameter. For the more stable regime, PDCs are observed throughout the entirety of the eruption. The dotted line represents the approximate transition between the stability regimes. The vent diameter labels indicate the input vent diameters for the eruptions plotted below them.

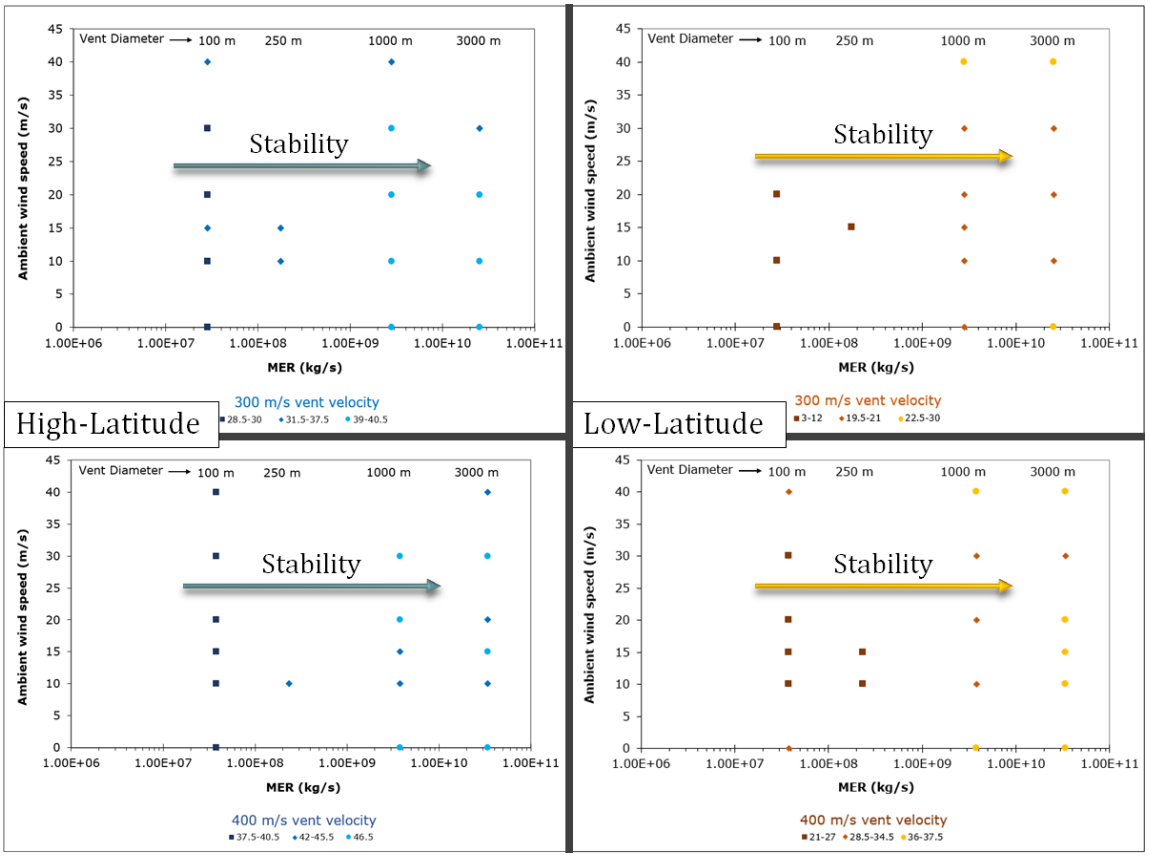

Figure 25: Plots of initially stable eruptions in both high- and low-latitudes. These figures compare eruption MER with the ambient wind velocity profiles and are categorized by first PDC collapse occurrence in minutes into the eruption. Three equal-interval categories are defined for each graph shown. As most of the initially stable eruptions occurred for initial vent exit velocities at or above 300 m/s, only the 300 and 400 m/s vent exit velocity eruptions are shown here. The vent diameter labels indicate the input vent diameters for the eruptions plotted vertically below them. In these initially stable eruptions, we observe an apparent trend of later PDC collapse times with increasing vent diameter and MER.

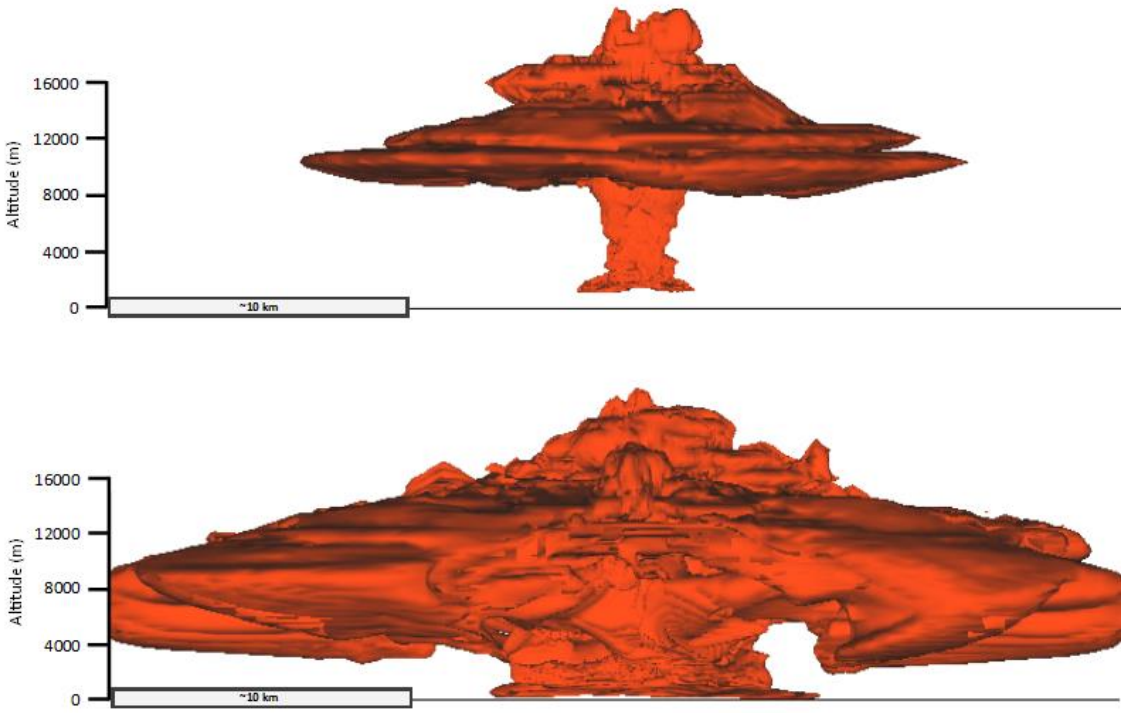

Figure 26: Example output of a total collapse in the altered warm-wet atmospheric profile. Input conditions for this example include 100 m/s vent exit velocity, 100 m vent diameter, and no-wind. This total umbrella collapse is not observed in the other atmospheric profiles. There were 4 total 3D simulations that showed this behavior, with input parameters of 100 and 1000 m vent diameter and 100 and 400 m/s vent exit velocity.

3.6: Discussion

Using over 150 simulations of volcanic eruptions in 2- and 3-D with ATHAM, we investigated the impact of specific parameters on the column collapse transition. Our results show that eruptions into peak wind velocities > 10 m/s can curve plume trajectories downwind (e.g., Bursik, 2001) and still produce PDCs that can travel further (by ~4 km) in the downwind direction compared to PDCs shed by equivalent eruptions in a no-wind environment; secondary PDCs can travel a few km in other directions in addition to the primary with-wind PDC. This has implications for hazard analyses to ensure consideration of an extended unidirectional PDC travel distance in the case of high wind speeds.

For unstable plumes, which make up most of our eruptions at 100-200 m/s vent velocities, we have shown that increasing wind velocity can transition partially unstable plumes to the fully unstable classification. However, it is important to note the differences in the wind velocity profiles used in this study. Between different wind profiles (e.g., 10, 20 m/s, etc.) the greatest wind speed difference is 10 m/s at tropopause height while near ground level the difference between profiles is ~1-2 m/s. For example, the 40 m/s wind profile has a 20 m/s wind speed at ~5 km asl. While these wind profiles are reasonable, they minimize the differences in wind speeds in the lower plume. Thus, in referring to the wind velocity profiles as they relate to this discussion, it is important to remember that the wind impacts may result from actually lower wind velocities since most of the eruption is experiencing slower wind speeds in the troposphere. Future works may consider using

alternative wind profiles, such as a uniform wind or higher near-ground winds. The 1D model of Degruyter and Bonadonna (2013) indicates that wind can stabilize plumes by increasing entrainment and plume dilution, thereby reducing the maximum height and preventing PDC generation. Our results show that even higher wind speeds during eruptions with MERs between 1E+07 – 1E+10 kg/s will lead to unstable plumes with continuous PDC generation and even extended PDC distances in the with-wind direction. This disparity is likely due to the different treatment of entrainment: while Degruyter and Bonadonna (2013) use a set of end-member entrainment coefficients from previous works to reduce the problem to 1D, ATHAM applies Navier-Stokes equations with a turbulence closure scheme to explicitly calculate turbulent entrainment. It is crucial to employ 2- and 3-D coordinate schemes to incorporate complex processes like column collapse (Neri and Macedonio, 1996) and turbulent entrainment (Herzog et al., 2003).

Natural eruptions of note that exhibited both column rise and PDCs within a wind field include the Cordón Caulle, Chile eruption in 2011. The eruption started on June 4, 2011, and produced a 9-12 km asl plume with wind speeds recorded ~30 m/s at 10 km asl and 20 m/s or less below 5 km asl (Bonadonna et al., 2015). During the first two days of the eruption approximately 5 PDCs were reported in addition to negligible upwind sedimentation (SERNAGEOMIN). The 1997 explosive activity from the Soufrière Hills volcano in Montserrat marks another example of partial instability in wind; nearly all of the vulcanian eruptions associated with the explosive phase were categorized as partially unstable. Throughout these eruptions an average two-thirds of the erupted material collapsed to form PDCs while the

remaining material was buoyed into the atmosphere, often reaching heights of ~12-13 km asl. Both the umbrella and lower plume were reported to have experienced significant winds (Druitt et al., 2002).

Our results from eruptions with large vent diameters show that PDCs form later with large vent sizes in initially stable plumes. While counter to conventional thought that large vent sizes induce plume instability, this apparent increase in stability was also shown with 3D numerical simulations by Suzuki and Koyaguchi (2012). The larger vent size produces a wider plume diameter, which prevents the inner core of the jet from becoming eroded by the annular mixing layer before the unmixed core loses its momentum. At the height at which the jet loses its momentum, the dense inner core spreads radially (e.g., Neri and Dobran, 1994; Lin and Armfield, 2000) and induces large-scale eddy mixing with the ambient air, and provides sufficient upward flow and buoyant rise as a stable column, referred to as a fountain-type column in Suzuki and Koyaguchi (2012). However, beyond some critical vent diameter, the radially expanded material cannot entrain enough air for the entire mixture to become buoyant, thus producing PDCs, referred to as fountain-type collapse (Suzuki and Koyaguchi, 2012), which aligns with convention of large vent sizes leading to less stable plumes and collapse. A real-world example of an eruption that collapsed after an initial period of stable rise is that of Vesuvius, Italy 79 A.D. One of the first phases of the eruption (EU2; Cioni et al., 1992) produced a plinian column that rose to ~25 km (Carey and Sigurdsson, 1987). This was followed by partial plume collapse and subsequent PDCs that inundated Herculaneum and Terzigno. There was a period of plume rise and partial collapse

before the full collapse that produced the radially dispersed PDC that reached Pompeii (Gurioli et al., 2002).

Most of our eruptions compare well with plume heights and MERs of ~35 real observations presented in Mastin et al. (2009). The primary deviation in our eruptions lie in our large MER (~10^{10} kg/s) eruptions, of which limited comparable observations or data are available in nature due to the rare occurrence of such explosive eruptions. As expected, maximum ash-cloud heights are greater in the warm-wet atmosphere owing to the higher tropopause height. However, we observe PDC collapse times later in the cold-dry atmosphere compared to their warm-wet counterparts. One potential explanation lies in the density differences in the ambient air between the warm and cold atmospheres. A colder, denser atmosphere has the capability for greater expansion once entrained and warmed by the eruption column. This greater expansion allows for a relatively greater buoyancy, which could be the reason for the later PDC collapses in the cold atmosphere.

Since temperature varied between our two profiles it is difficult to determine the degree of influence from atmospheric humidity alone. Preliminary investigation to test a rescaled tropopause height resulted in a full umbrella collapse condition not observed elsewhere in this study. This collapse condition occurred in a tropopause height of ~10 km with an increased temperature and relative humidity lapse rate compared to our original atmospheric profile. The average temperature lapse rate in this atmosphere is approximately -10 degrees C/km, with a tropopause temperature of -78.5 degrees C. The relative humidity varies with height but below

the tropopause it varies between 26 and 89.5%. Carazzo and Jellinek (2012) observed a similar time-dependent total umbrella collapse in their tank experiments, citing its observation as the first in known literature and attributes the cause to high particle concentrations and low flow rates. We encourage future workers with ATHAM to consider further investigations on the conditions for this relatively new total umbrella collapse scenario.

3.7: Conclusions

Results from our study using 2D- and 3D-ATHAM to evaluate the impact of atmospheric conditions on plume stability indicate several key findings: 1) high wind speeds can destabilize plumes, even those with large MERs; 2) larger vent diameters can have stabilizing effects, i.e., while the ratio of column circumference to cross-sectional vent area leads to decreased plume stability in no-wind environments, it instead serves to minimize the effects of extreme winds; and 3) while eruptions in a high-latitude atmosphere have dampened rise heights, they are stable for longer than identical eruptions in low-latitudes. This work has implications for the treatment of hazards in an operational setting by introducing the potential for wind-triggered collapse as well as stabilization (Kobs, 2009; Degruyter and Bonadonna, 2013). Thus, increased wind speeds during a volcanic crisis could either increase or decrease hazard risk. Not only could wind cause PDC generation, but PDCs from a wind-destabilized plume may travel further in the with-wind direction while the plume is still capable of shedding localized PDCs in other directions. Future ventures beyond this work should consider linking plume

morphologies presented here to their resultant deposition by using the depositional modules in ATHAM, with the goal of comparing with-wind deposits and plume morphologies to related literature (e.g., Carey and Sparks, 1986).

Chapter 4: Crucial Findings and Future Works

4.1: Key Findings

The key findings of this thesis include:

1) high wind velocities can destabilize plumes, even those with large MERs,

2) larger vent diameter eruptions can increase column stability, and

3) despite lower plume rise heights, high-latitude eruptions tend to produce PDCs later than in low-latitude eruptions.

4.2: Future Works

I recommend future work to build off of this research in the following ways: 1) testing the different impacts of relative humidity or testing different atmospheric profiles that do not have a large difference in relative humidity; 2) further constraining the transition between unstable and stable plumes, particularly for eruptions with smaller vent sizes; and 3) connecting plume morphologies observed here to deposit development using the deposition modules in ATHAM. The importance of these potential future works is summarized below.

1) In testing the impact of relative humidity, future workers should consider using a similar relative humidity profile between different atmospheres to specifically examine the impact of the ambient temperature on the plume without also varying the relative humidity. This method would allow for a more direct comparison between atmospheric profiles with different temperatures and, therefore, tropopause heights. While we know a lower tropopause height can

reduce the maximum height of a plume, we don't know much about the impact this dampened tropopause height may play in plume stability. One of the questions I was interested in with this thesis was whether the dampened tropopause height would reduce the ability for large scale entrainment in the atmosphere, however, results from my simulations were inconclusive on this point.

2) While this thesis completed a large suite of eruptions with various input conditions, further simulations with other input variables or values would build upon this work. For example, using a smaller vent diameter (~20-80 m) should give lower MERs, which is important to have since the lowest MER in this thesis was $\sim 10^7$ kg/s – considered a fairly high MER. Weight % of gas at the vent could be varied to something less than the 6 wt% in all my eruptions, since 6 wt% is usually on the higher end (ex. Figure 4 of Carazzo et al., 2008). I recommend using a 3 wt% of gas to compare with my work here.
3) Kobs (2009) presented a large pyroclast module (LPM) that allows ATHAM to track transport and deposition of large (> 1 cm) clast sizes. The original focus of my thesis was to compare deposition with the LPM module in a windy, 3D environment to the nomograms of Carey and Sparks (1986) in an attempt to bring the nomograms up to date using a 3D eruption simulator. However, issues with computer clusters and lack of time forced the thesis into a different direction. This is still a valuable direction to move towards and I would encourage consideration of this type of project.

4.3: Personal ATHAM Suggestions

ATHAM is a challenging code to use. To aid future users, particularly those pursuing the projects I suggest above, I offer several suggestions: 1) run simulations early and often; you never know when the machine you're running ATHAM on will break down, leaving you with a serious problem if your project relies on ATHAM; 2) understand the input variables as much as possible; learning the key variables you're using and how they impact eruptions will aid you immensely in defining what parameters you should be testing; 3) try to figure out the specifics of ATHAMs inner workings before too long; you want to make sure you know what ATHAM is doing while it is running as well as what its strengths and weaknesses are, and if you are mathematically inclined be sure to pay special attention to the equations of ATHAM (look in Oberhuber et al., 1998 and Herzog et al., 2003); and 4) consider long and hard the type of visualization software you want to use with the output you get from ATHAM. I used UNIDATA IDV, which does a pretty good job of visualizing the output fairly easily. However, if you are interested in something a bit more robust, then look into UCAR's Vapor. I tried to use it but I didn't have enough time to work with it to get any output to display. It requires a bit of post-processing and a regular grid instead of a stretched grid, according to my conversations with Alexa Van Eaton from USGS/Arizona State.

A quick-start guide for an earlier version of ATHAM can be found in the dissertation appendices of Kobs (2009), but here I will provide additional information for working with ATHAM per my experience. While I was running

simulations on the cluster supercomputer, I used PuTTY (http://www.putty.org/) and WinSCP (http://winscp.net/eng/index.php) to log in to the cluster. WinSCP allows for a more intuitive GUI to work with the files within ATHAM; it also allows an easy way to upload or update input files or download output files. These two programs are only for using ATHAM on a cluster, which is usually only for 3D. For 2D on a non-cluster or personal computer, it would probably be best to follow the startup instructions in Kobs (2009).

The input variables I changed the most in this work can be found in: ATHAM/input/…

- 'INPUT_atham_setup'
  - cylindric_geometry: .true. for 2D; .false. for 3D
  - nx, ny, nz: the number of grid points for each direction (set ny to 4 for 2D)
  - npx, npy: number of processors for these directions (set npy to 1 for 2D)
  - nrep: the number of times for output during eruption
  - period: the time in seconds during the eruption between each output (nrep)
  - no_uwind, no_vwind: set to .false. to turn on wind in this direction
- 'INPUT_profile'
  - This input file defines the atmospheric profile to use during the eruption. If you run the code without this file, ATHAM will use a default profile defined in the code.
- 'INPUT_volcano'
  - radtrac: These are the particle sizes. I didn't alter these, but future workers may find it useful to use different sizes.
  - eruption: this is the time in seconds that the eruption will last
  - damping: this is the time at which the eruption itself will stop
  - volcano_vwidth: the width of the crater rim
  - volvel: exit velocity of the vent in m/s
  - voltem: potential temperature at the vent (in k). I didn't change this but future workers may like to try changing this temperature for different results.

- voltgas and voltrac: These represent the specific concentrations of gas and particles, respectively, at the vent. The components of these two should add up to 1. Future workers should understand what realistic values would be before changing these. Also, the numbers in parentheses correspond to the particular tracer, relating to particle sizes, densities, etc. in other parts of INPUT_volcano.

4.4: Terms of numerical analysis used in this thesis

Large Eddy Simulation (LES):

The LES is a widely used numerical model for 3-D turbulence that integrates the spatial components of the equations of motion. Large-scale turbulent eddies are explicitly solved while small-scale eddies are approximated. This approach is required due to the massive amount of computational power that would be required to simulate turbulence at all scales, which is feasibly out of reach for today's computers. Jim Deardorff developed the LES technique in the late 1960s (Moeng and Sullivan, 2002)

Message Passing Interface (MPI):

MPI is a message-passing standardization for parallel computing in distributed memory computers. MPI is used across multiple programming languages and is used to send and receive messages between processors. The primary advantage of MPI is its de-facto standard status for communicating across processors, applications, and tools in an efficient implementation. One of the first papers discussing MPI is that of Walker (1994).

UNAVCO IDV:

For visualizing ATHAM output, I used the UNAVCO IDV (Integrated Data Viewer), which can read and visualize NetCDF files (see below). The information and installation page can be found at

http://www.unavco.org/software/visualization/idv/idv.html

Within the software, I used the output file 'netCDF_MOV.nc' (selected from within the 'Data Choosers' tab) and applied the 'Isosurface' display option under '3D Surface' in the 'Field Selector' tab. Users should be sure to check 'All Levels' under the 'Level' section. Then, clicking on Create Display will start the visualization. There are plenty of other display options to choose from; feel free to play with the others to get a feel for the program and the output. Be sure to not have multiple files open in the IDV at the same time, otherwise it will likely crash.

Network Common Data Form (NetCDF):

NetCDF is a data form for accessing and storing multidimensional data. The NetCDF data is useful for representing scientific data in independent data formats. The homepage for the NetCDF project is located under UNIDATA at:

http://www.unidata.ucar.edu/software/netcdf/

Non-Hydrostatic Model:

ATHAM is a non-hydrostatic model. This simply means that the hydrostatic approximation is not used so that the effects of vertical accelerations can be accounted for, which is important since we're mainly concerned with upward moving clouds of ash. In other words, it means that ATHAM doesn't ignore the vertical acceleration and Coriolis force in the equations of motion.

References

Atmospheric Soundings. (2015). University of Wyoming Radiosonde Data. Department of Atmospheric Sciences. Retrieved from http://weather.uwyo.edu/upperair/sounding.html

Barsotti, S., Neri, A., & Scire, J. S. (2008). The VOL-CALPUFF model for atmospheric ash dispersal: 1. Approach and physical formulation. *Journal of Geophysical Research: Solid Earth*, *113*(B3).

Bonadonna, C., & Costa, A. (2010). Modeling of tephra sedimentation from volcanic plumes. *Modeling Volcanic Processes: The Physics and Mathematics of Volcanism*.

Bonadonna, C., Phillips, J. C., & Houghton, B. F. (2005). Modeling tephra sedimentation from a Ruapehu weak plume eruption. *Journal of Geophysical Research*, *110*(B8), B08209. doi:10.1029/2004JB003515.

Bonadonna, C., Pistolesi, M., Cioni, R., Degruyter, W., Elissondo, M., & Baumann, V. (2015). Dynamics of wind-affected volcanic plumes: The example of the 2011 Cordón Caulle eruption, Chile. *Journal of Geophysical Research: Solid Earth*, *120*(4), 2242-2261.

Bursik, M. (1989). Effects of the drag force on the rise height of particles in the gas-thrust region of volcanic eruption columns. *Geophysical Research Letters*, *16*(5), 441–444.

Bursik, M. (2001). Effect of wind on the rise height of volcanic plumes. *Geophysical Research Letters*, *28*(18), 3621–3624. doi:10.1029/2001GL013393.

Bursik, M. I., & Woods, A. W. (1991). Buoyant, superbuoyant and collapsing eruption columns. *Journal of Volcanology and Geothermal Research*, *45*(3), 347-350.

Bursik, M. I., Kobs, S. E., Burns, A., Braitseva, O. A., Bazanova, L. I., Melekestsev, I. V., ... & Pieri, D. C. (2009). Volcanic plumes and wind: Jetstream interaction examples and implications for air traffic. *Journal of Volcanology and Geothermal Research*, *186*(1), 60-67.

Carazzo, G., & Jellinek, A. M. (2012). A new view of the dynamics, stability and longevity of volcanic clouds. *Earth and Planetary Science Letters*, *325*, 39-51.

Carazzo, G., Kaminski, E., & Tait, S. (2008). On the rise of turbulent plumes: Quantitative effects of variable entrainment for submarine hydrothermal vents, terrestrial and extra terrestrial explosive volcanism. *Journal of Geophysical Research: Solid Earth*, *113*(B9).

Carey, S. N., & Sigurdsson, H. (1982). Influence of particle aggregation on deposition of distal tephra from the May 18, 1980, eruption of Mount St. Helens volcano. *Journal of Geophysical Research: Solid Earth*, *87*(B8), 7061-7072.

Carey, S. N., & Sparks, R. S. J. (1986). Quantitative models of the fallout and dispersal of tephra from volcanic eruption columns. *Bulletin of Volcanology*, *48*(2-3), 109-125.

Carey, S. N., Sigurdsson, H., & Sparks, R. S. J. (1988). Experimental studies of particle-laden plumes. *Journal of Geophysical Research: Solid Earth*, *93*(B12), 15314-15328.

Carey, S., & Sigurdsson, H. (1987). Temporal variations in column height and magma discharge rate during the 79 AD eruption of Vesuvius. *Geological Society of America Bulletin*, *99*(2), 303-314.

Casadevall, T. J., Delos Reyes, P. J., & Schneider, D. J. (1996). The 1991 Pinatubo eruptions and their effects on aircraft operations. *Fire and Mud: eruptions and lahars of Mount Pinatubo, Philippines*, 625-636.

Chen, C. J., & Rodi, W. (1980). Vertical turbulent buoyant jets: a review of experimental data. *NASA STI/Recon Technical Report A*, *80*, 23073.

Cioni, R., Marianelli, P., & Sbrana, A. (1992). Dynamics of the AD 79 eruption: Stratigraphic, sedimentological and geochemical data on the successions from the Somma-Vesuvius southern and eastern sectors. *Acta Vulcanol*, *2*, 109-123.

Cioni, R., Sulpizio, R., & Garruccio, N. (2003). Variability of the eruption dynamics during a subplinian event: the Greenish Pumice eruption of Somma–Vesuvius (Italy). *Journal of volcanology and geothermal research*,*124*(1), 89-114.

Connor, C. B., Hill, B. E., Winfrey, B., Franklin, N. M., & Femina, P. C. L. (2001). Estimation of volcanic hazards from tephra fallout. *Natural Hazards Review*, *2*(1), 33-42.

Costa, A., Macedonio, G., & Folch, A. (2006). A three-dimensional Eulerian model for transport and deposition of volcanic ashes. *Earth and Planetary Science Letters*, *241*, 634–647. doi:10.1016/j.epsl.2005.11.019.

Costa, A., Suzuki, Y. J., Cerminara, M., Devenish, B. J., Ongaro, T. E., Herzog, M., ... & Engwell, S. (2016). Results of the eruptive column model inter-comparison study. *Journal of Volcanology and Geothermal Research*.

Degruyter, W., & Bonadonna, C. (2012). Improving on mass flow rate estimates of volcanic eruptions. *Geophysical Research Letters*, *39*(16).

Degruyter, W., & Bonadonna, C. (2013). Impact of wind on the condition for column collapse of volcanic plumes. *Earth and Planetary Science Letters*, *377*, 218-226.

Devenish, B. J. (2013). Using simple plume models to refine the source mass flux of volcanic eruptions according to atmospheric conditions. *Journal of Volcanology and Geothermal Research*, *256*, 118-127.

Druitt, T. H., & Kokelaar, B. P. (Eds.). (2002). The eruption of Soufrière Hills volcano, Montserrat, from 1995 to 1999. Geological Society of London.

Eisele, J. W., O'Halloran, R. L., Reay, D. T., Lindholm, G. R., Lewman, L. V., & Brady, W. J. (1981). Deaths during the May 18, 1980, eruption of Mount St. Helens. *The New England journal of medicine*, *305*(16), 931.

Ernst, G. G., Sparks, R. S. J., Carey, S. N., & Bursik, M. I. (1996). Sedimentation from turbulent jets and plumes. *Journal of Geophysical Research: Solid Earth (1978–2012)*, *101*(B3), 5575-5589.

Esposti Ongaro, T., Cavazzoni, C., Erbacci, G., Neri, A., & Salvetti, M. V. (2007). A parallel multiphase flow code for the 3D simulation of explosive volcanic eruptions. *Parallel Computing*, *33*(7), 541-560.

Esposti Ongaro, T., Neri, A., Todesco, M., & Macedonio, G. (2002). Pyroclastic flow hazard assessment at Vesuvius (Italy) by using numerical modeling. II. Analysis of flow variables. *Bulletin of volcanology*, *64*(3), 178-191.

Folch, A., Costa, A., & Macedonio, G. (2009). FALL3D: A computational model for transport and deposition of volcanic ash. *Computers & Geosciences*, *35*(6), 1334-1342.

Glaze, L. S., & Baloga, S. M. (1996). Sensitivity of buoyant plume heights to ambient atmospheric conditions: Implications for volcanic eruption columns. *Journal of Geophysical Research: Atmospheres (1984–2012)*, *101*(D1), 1529-1540.

Graf, H. F., Herzog, M., Oberhuber, J. M., & Textor, C. (1999). Effect of environmental conditions on volcanic plume rise. *Journal of Geophysical Research: Atmospheres (1984–2012)*, *104*(D20), 24309-24320.

Gurioli, L., Cioni, R., Sbrana, A., & Zanella, E. (2002). Transport and deposition of pyroclastic density currents over an inhabited area: the deposits of the AD 79 eruption of Vesuvius at Herculaneum, Italy. *Sedimentology*, *49*(5), 929-953.

Herzog, M., Graf, H., Textor, C., & Oberhuber, J. M. (1998). The effect of phase changes of water on the development of volcanic plumes, 55–74.

Herzog, M., Oberhuber, J. M., & Graf, H. F. (2003). A prognostic turbulence scheme for the nonhydrostatic plume model ATHAM. *Journal of the atmospheric sciences*, *60*(22), 2783-2796.

Hewett, T. A., Fay, J. A., & Hoult, D. P. (1971). Laboratory experiments of smokestack plumes in a stable atmosphere. *Atmospheric Environment (1967)*, *5*(9), 767-789.

Hoinka, K. P. (1999). Temperature, humidity, and wind at the global tropopause. *Monthly Weather Review*, *127*(10), 2248-2265.

Hurst, A. (1994). ASHFALL, a computer program for estimating volcanic ash fallout: report and users guide. Institute of Geological & Nuclear Sciences.

Hurst, A. W., & Turner, R. (1999). Performance of the program ASHFALL for forecasting ashfall during the 1995 and 1996 eruptions of Ruapehu volcano. *New Zealand Journal of Geology and Geophysics*, *42*(November 2013), 615–622. doi:10.1080/00288306.1999.9514865.

Kaminski, É., & Jaupart, C. (2001). Marginal stability of atmospheric eruption columns and pyroclastic flow generation. *Journal of Geophysical Research: Solid Earth (1978–2012)*, *106*(B10), 21785-21798.

Kaminski, É., Tait, S., & Carazzo, G. (2005). Turbulent entrainment in jets with arbitrary buoyancy. *Journal of Fluid Mechanics*, *526*, 361-376.

Kobs, S. (2009). Modeling particle motion and near-vent deposition in explosive volcanic eruptions. State University of New York at Buffalo.

Kotsovinos, N. E., & List, E. J. (1977). Plane turbulent buoyant jets. Part 1. Integral properties. *Journal of Fluid Mechanics*, *81*(01), 25-44.

Koyaguchi, T., & Suzuki, Y. (2011). 3-D Numerical Simulations of Eruption Clouds: Effects of Decompression/Compression and Cross-Wind on the Dynamics of Eruption Clouds. *Annual Report of the Earth Simulator Center April*, *2012*.

Lin, W., & Armfield, S. W. (2000). Direct simulation of weak axisymmetric fountains in a homogeneous fluid. *Journal of Fluid Mechanics*, *403*, 67-88.

Macedonio, G., Costa, A., & Folch, A. (2008). Ash fallout scenarios at Vesuvius: numerical simulations and implications for hazard assessment. *Journal of Volcanology and Geothermal Research*, *178*(3), 366-377.

Mastin, L.G., Guffanti, M., Servranckx, R., Webley, P., Barsotti, S., Dean, K., Durant, A., Ewert, J.W., Neri, A., Rose, W.I. and Schneider, D. (2009). A multidisciplinary effort to assign realistic source parameters to models of volcanic ash-cloud

transport and dispersion during eruptions. *Journal of Volcanology and Geothermal Research*, *186*(1), 10-21.

Mastrolorenzo, G., Petrone, P. P., Pagano, M., Incoronato, A., Baxter, P. J., Canzanella, A., & Fattore, L. (2001). Herculaneum victims of Vesuvius in AD 79. *Nature*, *410*(6830), 769-770.

Meertens, C. & Wier, S. (2007). UNAVCO Software and Services for Visualization and Exploration of Geoscience Data, Eos Trans. AGU, 88(52), Fall Meet. Suppl., Abstract IN33A-0872.

Meertens, C., L. D. Murray, & J. McWhirter. (2004). Collaborative Visualization and Analysis of Multi-dimensional, Time-dependent and Distributed Data in the Geosciences Using the Unidata Integrated Data Viewer, Eos Trans. AGU, 85(47), Fall Meet. Suppl., Abstract SF13A-0710.

Moeng, C. H., & Sullivan, P. P. (2002). Large eddy simulation. *Encyclopedia of Atmospheric Sciences*, *1140*, 1150.

Morton, B. R., Taylor, G., & Turner, J. S. (1956). Turbulent gravitational convection from maintained and instantaneous sources. *Proceedings of the Royal Society of London. Series A. Mathematical and Physical Sciences*, *234*(1196), 1-23.

Neri, A., & Dobran, F. (1994). Influence of eruption parameters on the thermofluid dynamics of collapsing volcanic columns. *Journal of Geophysical Research: Solid Earth*, *99*(B6), 11833-11857.

Neri, A., & Macedonio, G. (1996). Physical modeling of collapsing volcanic columns and pyroclastic flows. In *Monitoring and mitigation of volcano hazards* (pp. 389-427). Springer Berlin Heidelberg.

Neri, A., Esposti Ongaro, T., Macedonio, G., Todesco, M., & Gidaspow, D. (2003). Assessing pyroclastic density current hazard by using multiphase flow models. In *EGS-AGU-EUG Joint Assembly* (Vol. 1, p. 14770).

Oberhuber, J. M., Herzog, M., Graf, H.-F., & Schwanke, K. (1998). Volcanic plume simulation on large scales. *Journal of Volcanology and Geothermal Research*, *87*(1-4), 29–53. doi:10.1016/S0377-0273(98)00099-7.

Ogden, D. E., Glatzmaier, G. A., & Wohletz, K. H. (2008). Effects of vent overpressure on buoyant eruption columns: Implications for plume stability. *Earth and Planetary Science Letters*, *268*(3), 283-292.

Papanicolaou, P. N., & List, E. J. (1988). Investigations of round vertical turbulent buoyant jets. *Journal of Fluid Mechanics*, *195*, 341-391.

Ricou, F. P., & Spalding, D. B. (1961). Measurements of entrainment by axisymmetrical turbulent jets. *Journal of fluid mechanics*, *11*(01), 21-32.

Searcy, C., Dean, K., & Stringer, W. (1998). PUFF: A high-resolution volcanic ash tracking model. *Journal of Volcanology and Geothermal Research*, *80*(1-2), 1–16. doi:10.1016/S0377-0273(97)00037-1.

Servicio Nacional de Geología y Minería/Observatorio Volcanológico de Los Andes del Sur [SERNAGEOMIN]. (2011). Puyehue-Cordón Caulle: Reporte especial de actividad volcánica No. 31, Rep. [Available at http://www.sernageomin.cl/volcan.php?pagina=7&iId=38.]

Sparks, R. S. J. (1986). The dimensions and dynamics of volcanic eruption columns. *Bulletin of Volcanology*, *48*(1), 3-15.

Sparks, R. S. J., & Wilson, L. (1976). A model for the formation of ignimbrite by gravitational column collapse. *Journal of the Geological Society*, *132*(4), 441-451.

Sparks, R. S. J., Bursik, M. I., Carey, S. N., Gilbert, J. S., Glaze, L. S., Sigurdsson, H., & Woods, A. W. (1997). Volcanic Plumes, 574 pp.

Spence, R., Kelman, I., Brown, A., Toyos, G., Purser, D., & Baxter, P. (2007). Residential building and occupant vulnerability to pyroclastic density currents in explosive eruptions. *Natural Hazards and Earth System Science*, *7*(2), 219-230.

Suzuki, T. (1983). A theoretical model for dispersion of tephra. *Arc Volcanism, Physics and Tectonics*, 95–113.

Suzuki, Y. J., & Koyaguchi, T. (2010). Numerical determination of the efficiency of entrainment in volcanic eruption columns. *Geophysical Research Letters*, *37*(5).

Suzuki, Y. J., & Koyaguchi, T. (2012). 3-D numerical simulations of eruption column collapse: Effects of vent size on pressure-balanced jet/plumes. *Journal of Volcanology and Geothermal Research*, *221*, 1-13.

Suzuki, Y. J., Koyaguchi, T., Ogawa, M., & Hachisu, I. (2005). A numerical study of turbulent mixing in eruption clouds using a three-dimensional fluid dynamics model. *Journal of Geophysical Research: Solid Earth (1978–2012)*, *110*(B8).

Tanaka, H. L. (1994). Development of a prediction scheme for volcanic ashfall from Redoubt volcano, Alaska. In *Volcanic Ash and Aviation Safety: Proceedings of the First International Symposium on Volcanic Ash and Aviation Safety, US Geol. Surv. Bull* (Vol. 2047, pp. 283-291).

Textor, C., Ernst, G. G., Herzog, M., & Tupper, A. (2004). Potential of the ATHAM model for Use in air traffic safety. In *2nd International Conference on Volcanic Ash and Aviation Safety*.

Tilling, R.I., & Lipman, R.W. (1993). Lessons in reducing volcanic risk. *Nature* 364, 277-280.

Tupper, A., Textor, C., Herzog, M., Graf, H. F., & Richards, M. S. (2009). Tall clouds from small eruptions: the sensitivity of eruption height and fine ash content to tropospheric instability. *Natural Hazards*, *51*(2), 375-401.

Valentine, G. A., & Wohletz, K. H. (1989). Numerical models of Plinian eruption columns and pyroclastic flows. *J. Geophys. Res*, *94*, 1867-1887.

Van Eaton, A. R. (2012). Dynamics of large, wet volcanic clouds: The 25.4 ka Oruanui eruption of Taupo volcano (Doctoral Dissertation), New Zealand. Victoria University of Wellington, New Zealand.

Veitch, G., & Woods, A. W. (2000). Particle recycling and oscillations of volcanic eruption columns. *Journal of Geophysical Research: Solid Earth*,*105*(B2), 2829-2842.

Veitch, G., & Woods, A. W. (2002). Particle recycling in volcanic plumes. *Bulletin of Volcanology*, *64*(1), 31-39.

Walker, D. W. (1994). The design of a standard message passing interface for distributed memory concurrent computers. *Parallel Computing*, *20*(4), 657-673.

Webster, H. N., Thomson, D. J., Johnson, B. T., Heard, I. P. C., Turnbull, K. F., Marenco, F., Kristiansen, N. I., Dorsey, J. R., Minidin, A., Weinzierl, B., Schumann, U., Sparks, S. S. J., Loughlin, S. C., Hort, M., Leadbetter, S. J., Devenish, B., Manning, A. J., Witham, C., Haywood, J. M., and Golding, B. (2012). Operational prediction of ash concentrations in the distal volcanic cloud from the 2010 Eyjafjallajökull eruption. *Journal of Geophysical Research: Atmospheres*, *117*(D20).

Wilson, L. (1976). Explosive volcanic eruptions—III. Plinian eruption columns. *Geophysical Journal International*, *45*(3), 543-556.

Wilson, L., & Walker, G. P. L. (1987). Explosive volcanic eruptions-VI. Ejecta dispersal in plinian eruptions: the control of eruption conditions and atmospheric properties. *Geophysical Journal International*, *89*(2), 657-679.

Wilson, L., Sparks, R. S. J., & Walker, G. P. (1980). Explosive volcanic eruptions—IV. The control of magma properties and conduit geometry on eruption column behaviour. *Geophysical Journal International*, *63*(1), 117-148.

Wilson, L., Sparks, R. S. J., Huang, T. C., & Watkins, N. D. (1978). The control of volcanic column heights by eruption energetics and dynamics. *Journal of Geophysical Research: Solid Earth*, *83*(B4), 1829-1836.

Witham, C. S. (2005). Volcanic disasters and incidents: a new database. *Journal of Volcanology and Geothermal Research*, *148*(3), 191-233.

Woodhouse, M. J., Hogg, A. J., Phillips, J. C., & Sparks, R. S. J. (2013). Interaction between volcanic plumes and wind during the 2010 Eyjafjallajökull eruption, Iceland. *Journal of Geophysical Research: Solid Earth*, *118*(1), 92-109.

Woods, A. W. (1988). The fluid dynamics and thermodynamics of eruption columns. *Bulletin of Volcanology*, 169–193.

Woods, A. W. (1995). The dynamics of explosive volcanic eruptions. *Reviews of Geophysics*, *33*(4), 495-530.

Woods, A. W. (2010). Turbulent plumes in nature. *Annual Review of Fluid Mechanics*, *42*, 391-412.

Woods, A. W., & Bursik, M. I. (1991). Particle fallout, thermal disequilibrium and volcanic plumes. *Bulletin of Volcanology*, *53*(7), 559-570.

Wright, S. J. (1984). Buoyant Jets in Density-Stratified Crossflow. *Journal of Hydraulic Engineering*.

Yamamoto, K. (2002). *Numerical experiments and the assessment for the probability of the volcanic ash dispersal* (Doctoral dissertation, Master thesis, Graduate School of Life and Environmental Sciences, University of Tsukuba).